Giant, 29, 2026, 100412

Engineering 2D Bi_2WO_6 reinforced P(VDF-TrFE) nanocomposites for enhanced electronic stopping power and radiation efficiency

Full-length article

Nabil Janan Al-Bahnam[a], Rahman I. Mahdi[b], M.Kh. Hamad[c], M.I. Sayyed[d,e], Yasser Maghrbi[f,g,*], Kawa M. Kaky[h,i]

[a] Physics Department, College of Science for Women, University of Baghdad, Baghdad, 10071, Iraq
[b] Nanotechnology and Advanced Material Research Center, University of Technology-Iraq, Baghdad 10066, Iraq
[c] Department of Basic Sciences, School of Social and Basics Sciences, Al Hussein Technical University, King Abdullah II St 242, Amman 11831, Jordan
[d] Department of Physics, Faculty of Science, Isra University, Amman, Jordan
[e] Department of Physics, Dogus University, Dudullu-Ümraniye, 34775, Istanbul, Türkiye
[f] Gulf University for Science and Technology, Department of Mathematics and Natural Sciences, Kuwait
[g] Université Côte d'Azur, Observatoire de la Côte d'Azur, CNRS, Laboratoire ARTEMIS, Nice, 06300, France
[h] Department of Medical Equipment Engineering, College of Engineering Technologies, Al-Nisour University, Baghdad, Iraq
[i] Department of Radiology and Sonography, College of Health & Medical Technologies, Al-Nisour University, Baghdad, Iraq

Keywords: P(VDF-TrFE)-Bi_2WO_6, Nanocomposite, Stopping power, Radiation shielding, Lead-free materials

Growing environmental concerns and the increasing restrictions on toxic heavy–metal–based shielding materials have accelerated the development of sustainable lead-free materials. In this study Bi_2WO_6 nanosheets were incorporated into a P(VDF-TrFE) copolymer at different weight percentages (wt%) ranging from 1 to 10 wt% to fabricate P(VDF-TrFE)-Bi_2WO_6 flexible composite system with enhanced functional performance. X-ray diffraction (XRD) and Fourier transform infrared (FTIR) spectroscopy were used to confirm the crystalline structure and vibrational modes of P(VDF-TrFE)-Bi_2WO_6 nanocomposite. The microstructure analysis confirms that the Bi_2WO_6 nanosheets were well dispersed in the P(VDF-TrFE) host. Introducing the Bi_2WO_6 sheet in P(VDF-TrFE) host strengthens the electrical response, reducing bulk plasmon energy from 24.72 to 21.5 eV and increasing mean excitation energy from 120.7 to 221 eV, increases stopping power, and slows down charge particles, with the smallest projected range PR to absorb protons and ^{3}Li ions, notably at 10 wt% based on SRIM computations. Photon shielding performance was quantified for all polymer composites by simulating the linear attenuation coefficient (μ) over 0.015 MeV – 15 MeV energy range using Geant4 MC toolkit. The results

* Corresponding author at: College of Arts & Sciences, Gulf University for Science and Technology, Hawally, Kuwait.
E-mail addresses: nabiljb_phys@csw.uobaghdad.edu.iq, nabeil.physic@gmail.com (N.J. Al-Bahnam), yasser.maghrbi@univ-cotedazur.fr (Y. Maghrbi).
Received 23 May 2026; Received in revised form 8 July 2026; Accepted 27 July 2026

 https://doi.org/10.1016/j.giant.2026.100412

are then compared with theoretical data computed through Phy-X/PSD software. Excellent agreement was achieved across the full energy range, with average percentage differences $\overline{\Delta\%}$ of 0.209% to 0.566%, and a Goodness-of-Fit (χ^2) of 5.81×10^{-5} to 4.35×10^{-2} confirming that the Geant4 setup reproduces the theoretical μ values with high fidelity.

1 Introduction

The search for radiation shielding materials has been the order of the day in recent decades because of the dangers posed by ionizing radiation [1–3]. Polymers in this regard have been suggested by many researchers as potential radiation shielding materials because of it non-toxic and lightweight nature. Polymers have the advantage of systematically holding heavy particles in place whenever modernization is required. Polymers are very easy to work with when compared to conventional shielding materials in times of flexibility and also could be of great advantage especially in space exploration where weight management is required [4–6].

Most at times, in order to improve the thermal stability, resistance to radiation, and mechanical characteristics, copolymers are utilized instead of homopolymers. In order to create a highly durable material, different monomers could be combined together to form a single copolymer with good mechanical advantage. Copolymers composing of fluorinated or aromatic groups could offer an enhanced thermally stable material, subsequently providing a high temperature shielding characteristics. Copolymers could also be fabricated to oppose the degradations caused by radiation, making the composites structurally stable [7].

Precisely, the presence of high content of fluorine in copolymers like vinylidene fluoride (VDF, $C_2H_2F_2$) and trifluoro ethylene (TrFE, C_2HF_3) monomers could give a huge contribution to the enhancement of its electromagnetic shielding performance. This is because, the relatively high density of the fluorine atomic which contributes in absorbing radiation. Moreover, copolymers could be polarized because of its ferro electrical characteristics, and this increased its conductivity caused by radiation as well as shielding effectiveness. Poly(vinylidene-fluoride-trifluoroethylene-chlorotrifluoroethylene) (P(VDF-TrFE)) is well known as an electroactive ferroelectric polymer with piezoelectric behaviour, making it attractive for several functional applications. Its polar structure and spontaneous polarization can support electromechanical response which is why P(VDF-TrFE)-based materials are widely used in sensors, energy-harvesting systems, and flexible electronic devices [8,9]. Furthermore, in medical devices, atomic and nuclear industries, charges generated by radiation could be trapped by P(VDF-TrFE), thereby reducing the rate at which radiation transmits [10]. However, scientists and engineers working in the operational surroundings starting from fission and fusion nuclear reactor cores to high-energy particles while staying near the hazard radiation zone these functional materials are frequently exposed to complicated doses of ionizing radiation. These doses come from light ions (H, He, Li) and swift heavy ions($Z > 4$) which deposit high energy and initiate cascades of medium damage. At higher energy, the swift heavy ion beams striking heavy metals such as (Mo, W and Bi) can generate a secondary reaction called nuclear spallation, which spatters ejected (neutrons, protons, and pions) in all directions. Instead, workers are shielded by thick layers of polymer, concrete, materials with high hydrogen mass fractions like specialized Perovskite Oxyhydrides, which slow the movement of the charged particles in matter. As an energetic ion crosses the material, it slows down mainly via inelastic collisions with the atomic target's electrons, this interaction quantified by the electronic stopping power S_e (eV/Å). This quantity is needed to describe the spatial distribution of deposited ion energy and the morphology of any induced damage, like formation of latent trajectories in dielectric materials, then the energy loss events along the projectile's track determine the projected range (PR) and characterize the depth and volume of the irradiated material. The stopping power is not simplistic formula for the ion's bare nuclear charge, because it is dependent on the projectile's effective charge, which changes statistically as the projectile experiences random processes of electron capture and loss within the target medium [11].

A large body of literature has been committed to parameterizing these interactions, leading to utilized semi-empirical software such as SRIM (Stopping and Range of Ions in Matter) [12]. SRIM code is based on a Monte Carlo simulation strategy employing the binary collision approximation and Bragg's additivity rule for compounds [13], mixed gas [14] and solid stack layers [15,16].

High-proton doses obtain deeply restructuring the ferroelectric morphology of P(VDF–TrFE), leading to dose-dependent transformation from ferroelectric phase to a relaxor- ferroelectric state distinguished by slim polarization hysteresis loop [17]. Swift heavy-ion engineering transforms PVDF and (0.8) PVDF/$BaTiO_3$ (0.2) nanocomposite films into versatile, high-rate performance supercapacitor separators by correspondingly rewriting structure pore and crystal chemistry. Thin films irradiated by 80 MeV O^{6+} and 40 MeV Li^{3+} ion beams lead to phase transition $\alpha \rightarrow \beta$ in PVDF and substantially amorphized $BaTiO_3$. Under Li^{3+} ion irradiation, PVDF stopping and range results $S_e = 73.3$ eV/Å and PR = 0.074 mm, while the (0.8) PVDF/$BaTiO_3$ (0.2) composite results $S_e = 60.6$ eV/Å and PR = 0.094 mm. Under O^{6+} ion irradiation, PVDF has $S_e = 10$ eV/Å and PR = 0.229 mm, while the (0.8) PVDF/$BaTiO_3$ (0.2) has $S_e = 8.4$ eV/Å and PR = 0.284 mm [18].

Over the last 30 years, many studies have tied energy loss by ions to make modifications in the morphological and dielectric properties of (PVDF-TrFE). To the best of our knowledge, the electronic stopping power and range ion in (PVDF-TrFE) polymer reinforced by Bi_2WO_6 ceramic has not been examined intensely. Nevertheless, this work presents a significant synthesis of the experimental and computerized simulation challenges in knowledge of ion-dielectric interactions within these nanocomposite materials.

In recent years nanotechnology has attracted increasing attention in gamma radiation shielding due to the ability of nanomaterials to improve filler dispersion, interfacial interaction, and attenuation performance within polymer-based composites. Materials like nanoparticles are currently the game-changer when dealing with gamma radiation shielding. These particles are often used in a composite in order to improve the radiation absorption characteristics of the resulting composites because of their high density and superior atomic number (Z) [19–21]. Some of the nanoparticles has the characteristics of enhancing the optical transparency, the mechanical strength, and even the structural integrity of composite materials. Nanoparticles absorbs gamma radiation more effectively because of its superior surface area-to-volume ratio [22–25].

Nanoparticle like bismuth oxide (Bi_2O_3), because of its superior density (8.9 g/cm^3) and high proton number (Z = 83), has the ability to enhance some properties of material such as density and effective atomic number (Z_{eff}) [26]. These two parameters are the two major enhancers of radiation absorption, confirming that, shielding materials which have been doped with heavy metal oxides could have a better radiation shielding capability [27,28]. Thermal stability and structural integrity of a material could also be enhanced by incorporating Bi_2O_3 into copolymer material. The high atomic number (Z = 74) and superior density (7.2 g/cm^3) of tungsten oxide (WO_3) could also contribute immensely in improving some characteristics of copolymer like effective atomic number (Z_{eff}) and overall copolymer density. Added to that, tungsten oxide (WO_3) with its high melting point has the ability to improve the temperature resistance of the copolymer material which it is incorporated into [29]. Another interesting compound that does well potentially in gamma radiation shielding enhancement is bismuth tungstate (Bi_2WO_6). This compound is also known for its photo-catalytic properties, making it suitable for diverse applications such as pollutant degradation and water spilling. The photoinduced response of Bi_2WO_6-based materials is mostly determined by their electronic band structure. When irradiated with photon energy equal to or greater than the band gap, electrons are stimulated from the valence band to the conduction band, leaving holes in the valence band. Then, the photo-generated electrons and holes drive the subsequent reduction and oxidation events at the surface of the material. Thus, the band gap, band-edge positions and charge carrier separation/recombination behavior are the main parameters controlling the photocatalytic activity [30].

In PVDF-based composites, interfacial modification is known to play an important role in controlling composite morphology and functional response. Previous studies have shown that processing and interface control in and P(VDF-TrFE)-based systems can greatly affect structure and performance, while ceramic incorporation can also alter wettability, porosity, and matrix–filler interactions. Moreover, immediate surface functionalization of ceramic fillers has been reported to improve filler dispersion in PVDF matrices. Therefore, although the present work was focused on the composition-dependent functional and shielding properties of P(VDF-TrFE)/Bi_2WO_6 composites, surface modification of Bi_2WO_6 represents an important route for future optimization of filler distribution and interfacial compatibility [31–33].

In order to assess the materials shielding performance, most authors encouraged theoretical predictions, the mass and linear attenuation coefficients (MAC and LAC) of the material is predicted by defining its density and chemical composition in the case of Phy-X online friendly simulation software. The software also predicts data for the half and tenth value layers (HVL and TVL), mean free path (MFP), and effective atomic number (Z_{eff}). These parameters are used in predicting the radiation shielding behavior of a material effectively [34–37].

Considering the combined effects of fluorine in P(VDF-TrFE), and Bi_2WO_6, this research intends to theoretically investigates the gamma radiation shielding capability of P(VDF-TrFE)-Bi_2WO_6 copolymer-nanocomposites. The P(VDF-TrFE) used in this work has a composition of 75/25 with chemical formula for the poly (vinylidene fluoride-co-trifluoro-ethylene) (P(VDF-TrFE)) copolymer as $(C_2H_2F_2)_{0.75}(C_2HF_3)_{0.25}$. Bi_2WO_6 nanosheets will be added at different weight percentages of 0, 2, 4, 6, 8, and 10 wt% relative to the P(VDF-TrFE) polymer to produce P(VDF-TrFE)-Bi_2WO_6 nanocomposites.

2 Experimental and simulation

2.1 Synthesis of Bi_2WO_6 nanosheets

The fused molten technique has been employed to synthesize the Bi_2WO_6 nanosheets. Sodium tungstate ($Na_2WO_4{\cdot}2H_2O$), with a purity of 99.0% supplied by Apollo Scientific (UK), and bismuth nitrate ($Bi(NO_3)_3{\cdot}5H_2O$), with a purity of 99.9% supplied by Stanford Advanced Materials (USA). Chemically balanced amounts of $Bi(NO_3)_3{\cdot}5H_2O$ and $Na_2WO_4{\cdot}2H_2O$ were precisely weighted. Potassium nitrate (KNO_3) and sodium nitrate ($NaNO_3$), purity ≥ 99% were supplied by Shanghai Yixin Chemical (China). The $NaNO_3$ and KNO_3 salts were mixed in a 1:1 wt ratio. The mixture was subsequently ground using a planetary ball mill for 2 h to provide a homogeneous, well mixed composition, enhancing the interaction between the reactants. Following grinding, the mixtures, comprising salts and raw materials, were placed in a high purity 99.5% alumina crucible with a cover and subsequently calcined in a muffle furnace at a ramp rate of 2 degrees per minute, sustained at a temperature of 400 °C for 5 h. The resultant solid powder was naturally at room temperature upon calcination. The powders were then washed several times with ethanol to remove all soluble salts. The resultant catalysts were subsequently dried overnight at 80 °C to obtain Bi_2WO_6 nanosheets.

2.2 Synthesis of P(VDF-TrFE)-Bi_2WO_6 nanocomposites

P(VDF-TrFE)-Bi_2WO_6 nanocomposite films were fabricated by the drop casting route. The P(VDF-TrFE) with a 75/25 composition was obtained from Piezotech Arkema (France). Methyl ethyl ketone (MEK) supplied by Merck (Germany). To prepare the casting solution, a 5 wt% of P (VDF-TrFE) copolymer was dissolved in 10 ml of MEK solvent and sealed in glass vials. The vials were kept under stirring for 2 h at 70 °C until the P(VDF-TrFE) fully dissolved and a clear, transparent solution was obtained. After that, Bi_2WO_6 nanosheets were added at different weight percentages of 0, 2, 4, 6, 8, and 10 wt% relative to the P(VDF-TrFE) to produce P(VDF-

TrFE)-Bi_2WO_6 nanocomposites. The mixture was stirred for 3 h, then subjected to probe sonication at a temperature of 60 °C and probe power of 50 W to break agglomerates and promote uniform dispersion of the nanosheets in the polymer solution. The composite solutions were then stirred for an additional 20 min to maintain homogeneity. The final mixture was poured onto a clean glass Petri dish and left in a dry oven at 50 °C overnight until the MEK completely evaporated. The resulting freestanding films were removed carefully and their thickness was measured at several points using a precision micrometer. The average thickness was about 50 μm with an error of ±2 μm.

2.3 Characterization

The crystalline structure of materials was evaluated by X-ray diffraction (Bruker D8 Advanced, Germany) using a Kα target with a 2θ range from 10 to 80° Chemical bonds were evaluated by Fourier transform infrared spectroscopy (FTIR) using a Shimadzu IRTracer-100 (Japan). The morphologies of the samples were recorded using a field emission scanning electron microscope (FESEM) (Zeiss Ultra 55, Germany).

2.4 Electronic stopping powers theory

2.4.1 Energy loss and range ions

Electronic stopping powers for the prepared shields were calculated using the SRIM software for ion energies up to 100 MeV. The linear electronic stopping within the Bethe–Bloch formalism is written as:

$$S_e(eV/) = \kappa \frac{Z_{ion}^2}{\beta^2} L(\beta) \tag{1}$$

Where κ is the material-specific pre-factor constant, $\kappa = 3.07075 \times 10^{-3}\ \rho(\mathrm{gm/cm^3})\ Z_t/A$, Z_{ion} is the atomic number of the ion, Z_t is the atomic number of the material, β is the projectile's velocity as a fraction of the speed of light C, and A is the mass number. The stopping number expansion $L(\beta)$ included all the corrections to the ion and target energy loss process:

$$L(\beta) = L_0(\beta) + Z_{ion}L_{ion}(\beta) + Z_{ion}^2 L_t \tag{2}$$

The term $L_0(\beta)$ includes all the correction factors of the Fano equation, such as shell correction C/Z_t, mean ionization energy $\langle I \rangle$, the density effect or polarization effects in the target $\delta/2$, and relativistic terms $f(\beta)$. The value of the stopping number $L_0(\beta)$ can be calculated using

$$L_0(\beta) = f(\beta) - \frac{C}{Z_{ion}} - \ln\langle I \rangle - \frac{\delta}{2} \tag{3}$$

The 2nd term correction, $L_{ion}(\beta)$, refers to Barkas correction of the projectile, and the 3rd term correction, $L_2(\beta)$, refers to Bloch's correction of the target material [38]. The projected range is the distance a charged particle travels through a material before it stops. This quantity is related to the total stopping power (both electronic $S_e(E)$ and nuclear $S_n(E)$), as outlined below [39],

$$R = \int_0^R dx = \int_0^E \frac{dE}{[S_e(E) + S_n(E)]} \tag{4}$$

2.4.2 Mapping effective charge at equal projectile velocity

To enable quantified, matrix-to-matrix comparability of the charge state of Li ions, we calculated the electronic stopping power within effective charge $Z_{eff}(\upsilon)$ by normalizing the stopping power of Li ions to that of protons travelling at the same velocity ($\beta = \upsilon/C$) at the same weight fraction. This procedure is inherent in the confirmed charge state and stopping power concepts, where the energy loss of swift ions in a random stopping medium is characterized through a velocity-dependent effective charge, which includes dynamical screening and charge-exchange interactions along the projectile trajectory [40–42]. For ions moving at the same weight fraction and the same velocity, the effective charge of the proton $Z_{eff}(\upsilon)_p$ is approximately unity, and the effective charge of the lithium $Z_{eff}(\upsilon)_{Li}$ may be expressed as

$$Z_{eff}(\upsilon)_{Li} = Z_{eff}(\upsilon)_p \sqrt{\frac{S_e(\upsilon)_{Li}}{S_e(\upsilon)_p}} \tag{5}$$

Where $S_e(\upsilon)_{Li}$ and $S_e(\upsilon)_p$ correspond to the electronic stopping powers for Li and proton, respectively, were obtained from SRIM-2013, for lithium and proton in each examined shield composition. SRIM supplies stopping data in terms of kinetic energy for each projectile type. Since the effective-charge formalism above needs a comparison at the same velocity, the proton energy that yields the same β as a given Li ion energy must be explicitly calculated. For each Li energy in E_{Li}(MeV), the relativistic kinematics were determined by calculating the Lorentz factor γ and the reduced velocity β from the Li rest mass $M_{Li}(MeV/C^2)$ via:

$$\gamma_{Li} = 1 + \frac{E_{Li}}{M_{Li}C^2} \tag{6}$$

$$\beta_{Li} = \sqrt{1 - \frac{1}{\gamma_{Li}^2}} \tag{7}$$

When $\gamma_p = \gamma_{Li}$, the proton energy E_p corresponding to the same β_{Li} can be written as

$$E_p(\beta_{Li}) = (\gamma_{Li} - 1)M_pC^2 \tag{8}$$

Where M_p is the proton rest mass. The lithium effective charge as a function of lithium energy can be expressed equivalently as

$$Z_{eff}(E_{Li}) = \sqrt{\frac{S_e(E_{Li})_{Li}}{S_e(E_p(\beta_{Li}))_p}} \tag{9}$$

2.5 Radiation shielding features

The linear attenuation coefficient (μ) was determined for each sample using the Geant4 MC toolkit (v 4.11.0) compiled on Windows 11 PC. The simulation was created to simulate a narrow-beam transmission geometry in an air-filled world volume using "G4_AIR,". The geometry was carefully inspected using the Qt interface (version 6.5.3) to ensure the setup behaved as intended. Fig. 1 illustrates how the Qt was integrated into the Geant4 framework to visualize and validate the geometry. For every run, 10^6 monoenergetic photons (Green trajectories) with energies ranging from 15 keV and 15 MeV were directed toward the target sample (Cyan). Additionally, the transmitted photons were collected for data acquisition using a collimated sodium iodine (NaI) detector (Magenta). In order to guarantee a pencil-like beam profile and reduce the detection of scattered radiation, two lead (Pb) collimators (Gray), each with an inner radius of 0.25 cm, were finally placed along the beam axis.

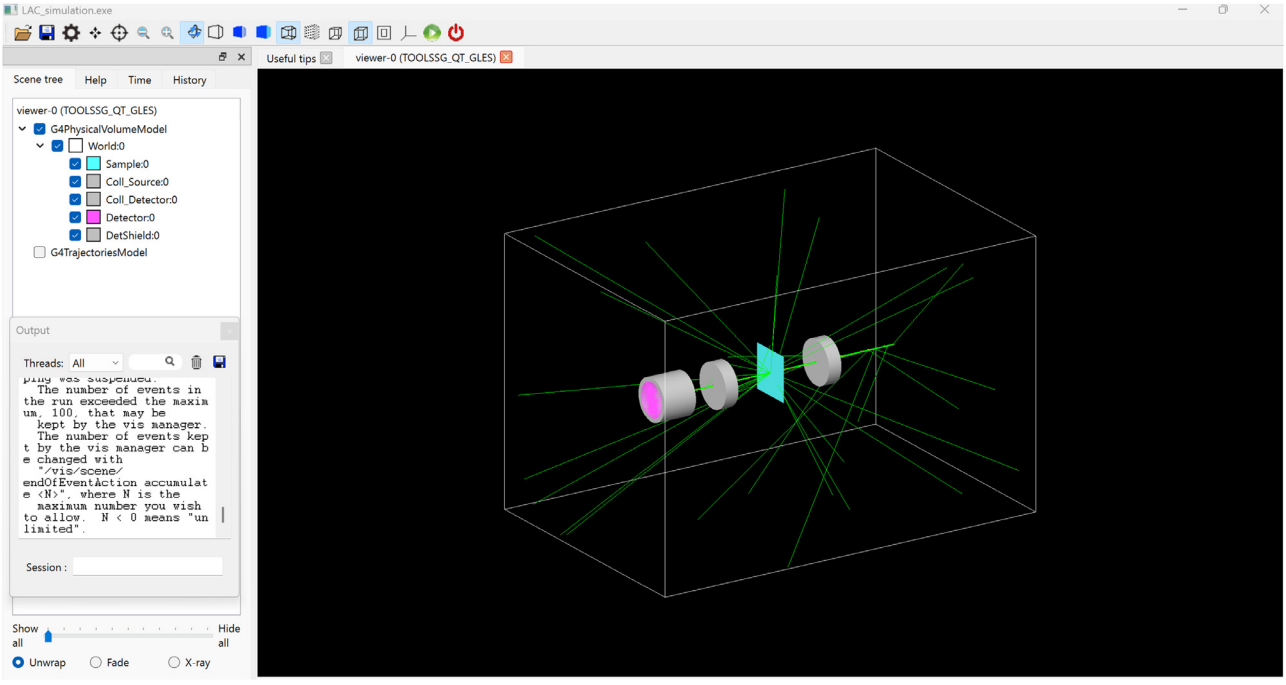

Fig. 1

3D visualization of the geometry setup using the Geant4 MC toolkit. The geometry includes the primary photon source (Green trajectories), lead collimators (Gray), the target sample (Cyan), and a shielded NaI detector (Magenta).

The "*G4EmStandardPhysics_option4*" physics list controlled the physics procedures. The most accurate modeling of electromagnetic interactions, including pair production, Compton scattering, Rayleigh scattering, and the photoelectric effect, is offered by this constructor. Furthermore, in order to strike a balance between computational efficiency and spatial precision, a global production cut for secondaries was set at 0.1 mm. The data acquisition was limited to primary photons identified by "*Track ID* $==1$ and "*Parent ID* $==0$" in order to guarantee the computation of the narrow-beam μ and eliminate secondaries.

The fundamental principle used to determine the simulated μ is based on the Beer-Lambart law:

$$\mu = \frac{1}{t}\ln\left(\frac{N_0}{N}\right) \tag{10}$$

Where t is the sample thickness in cm, N_0 and N are the number of primary photons (with *Track ID* $==1$, *and Parent ID* $==0$) reach the NaI detector before and after inserting the investigated sample, respectively.

The results are then benchmarked with theoretical data obtained using Phy-X/PSD software, which utilizes the NIST XCOM database and reported in Table 1. The reliability of the simulated data was assessed using different protocols including the percentage difference ($\Delta\%$) which helps in quantifying the relative deviation between the simulated (μ_{sim}) and theoretical (μ_{theo}) using:

$$\Delta\% = \left|\frac{\mu_{sim} - \mu_{theo}}{\mu_{theo}}\right| \times 100\% \tag{11}$$

Furthermore, the Chi-square (χ^2) test was utilized as a Goodness-of-Fit test to evaluate the statistical consistency between the two datasets according to:

$$\chi^2 = \sum_{i=0}^{n} \frac{(\mu_{sim,i} - \mu_{theo,i})^2}{\mu_{theo,i}} \tag{12}$$

Where $\mu_{sim,i}$ and $\mu_{theo,i}$ are the μ obtained from the Geant4 and Phy-X/PDS respectively for the i^{th} energy point, n is the total number of energy points ranging from 15 keV to 15 MeV. It is worth mentioning that a lower χ^2 value indicates a higher degree of correlation between the two datasets.

Finally, different key shielding parameters were calculated based on the obtained μ values such as the half-value layer (HVL), mean-free path (MFP), effective atomic number (Z_{eff}), transmission factor (TF), and radiation protection efficiency (RPE). These indicators give a clearer understanding of each sample's behavior when exposed to photons over the selected broad energy spectrum, and they allow direct comparison with published shielding materials. These parameters can be obtained according to the following equations:

$$HVL = \frac{\ln(2)}{\mu} \tag{13}$$

$$MFP = \frac{1}{\mu} \tag{14}$$

$$Z_{eff} = \frac{\sigma_a}{\sigma_e} \tag{15}$$

Where σ_a and σ_e are the total atomic and electronic cross-sections respectively.

The transmission factor (TF), and radiation protection efficiency (RPE) can be calculated using:

$$TF = \frac{N}{N_0} = e^{-\mu \times t} \tag{16}$$

Table 1

Linear attenuation coefficient (μ, cm^{-1}) of the investigated polymer composites (0–10 wt%) calculated using Geant4 (μ_{sim}) and Phy-X/PSD (μ_{theo}) over 0.015–15 MeV, together with the percentage difference (Δ%) between both datasets.

Energy (MeV)	μ (cm^{-1})																	
	0 wt%			2 wt%			4 wt%			6 wt%			8 wt%			10 wt%		
	μ_{theo}	μ_{sim}	Δ%	μ_{theo}	μ_{sim}	Δ%	μ_{theo}	μ_{sim}	Δ%	μ_{theo}	μ_{sim}	Δ%	μ_{theo}	μ_{sim}	Δ%	μ_{theo}	μ_{sim}	Δ%
0.015	2.668	2.662	0.239	6.589	6.578	0.158	10.631	10.680	0.457	14.763	15.126	2.461	19.021	18.608	2.170	23.404	23.357	0.201
0.02	1.292	1.297	0.352	3.903	3.907	0.099	6.605	6.622	0.263	9.369	9.163	2.192	12.217	11.570	5.297	15.150	15.150	0.002
0.03	0.598	0.599	0.290	1.516	1.520	0.248	2.464	2.465	0.065	3.432	3.438	0.170	4.431	4.440	0.221	5.458	5.469	0.188
0.04	0.426	0.426	0.001	0.863	0.862	0.165	1.312	1.309	0.229	1.771	1.766	0.233	2.242	2.241	0.055	2.728	2.727	0.053
0.05	0.359	0.358	0.296	0.607	0.605	0.262	0.859	0.855	0.385	1.115	1.111	0.353	1.379	1.370	0.603	1.650	1.644	0.387
0.06	0.325	0.324	0.295	0.482	0.480	0.478	0.640	0.635	0.776	0.800	0.794	0.736	0.964	0.954	1.057	1.133	1.122	0.967
0.08	0.290	0.290	0.005	0.426	0.425	0.255	0.563	0.561	0.422	0.702	0.699	0.414	0.844	0.839	0.607	0.991	0.983	0.752
0.1	0.269	0.269	0.096	0.443	0.442	0.219	0.619	0.617	0.302	0.798	0.796	0.219	0.983	0.980	0.224	1.172	1.166	0.546
0.15	0.237	0.236	0.365	0.303	0.302	0.213	0.367	0.367	0.082	0.432	0.432	0.008	0.498	0.498	0.015	0.566	0.565	0.121
0.2	0.216	0.216	0.146	0.251	0.250	0.137	0.283	0.282	0.246	0.315	0.314	0.090	0.347	0.348	0.101	0.381	0.381	0.049
0.3	0.187	0.186	0.512	0.203	0.203	0.130	0.217	0.217	0.025	0.229	0.229	0.196	0.242	0.242	0.166	0.256	0.256	0.041
0.4	0.167	0.167	0.229	0.178	0.178	0.276	0.186	0.186	0.061	0.193	0.193	0.208	0.201	0.200	0.083	0.208	0.208	0.153
0.5	0.153	0.153	0.047	0.161	0.161	0.072	0.167	0.166	0.332	0.172	0.171	0.251	0.177	0.177	0.018	0.182	0.181	0.325
0.6	0.141	0.141	0.168	0.148	0.147	0.477	0.153	0.153	0.045	0.156	0.156	0.341	0.160	0.160	0.419	0.164	0.163	0.538
0.8	0.124	0.124	0.094	0.129	0.129	0.151	0.133	0.132	0.286	0.135	0.135	0.390	0.138	0.138	0.392	0.141	0.140	0.355
1	0.111	0.111	0.384	0.116	0.116	0.457	0.119	0.118	0.332	0.121	0.121	0.208	0.123	0.123	0.193	0.125	0.125	0.503
1.5	0.091	0.090	0.386	0.094	0.094	0.386	0.096	0.096	0.537	0.098	0.097	0.615	0.100	0.099	0.589	0.101	0.100	0.658
2	0.078	0.077	0.480	0.081	0.081	0.186	0.083	0.083	0.349	0.084	0.084	0.464	0.086	0.085	0.600	0.087	0.086	0.654
3	0.063	0.063	0.199	0.065	0.065	0.461	0.067	0.067	0.361	0.068	0.068	0.238	0.070	0.069	0.275	0.071	0.071	0.173
4	0.054	0.054	0.041	0.056	0.056	0.186	0.058	0.058	0.213	0.059	0.059	0.306	0.060	0.060	0.108	0.062	0.062	0.158
5	0.048	0.048	0.120	0.050	0.050	0.302	0.052	0.052	0.182	0.053	0.053	0.017	0.055	0.055	0.109	0.056	0.056	0.014
6	0.044	0.044	0.030	0.046	0.046	0.005	0.048	0.048	0.198	0.049	0.049	0.209	0.051	0.051	0.066	0.052	0.052	0.102
8	0.039	0.039	0.323	0.041	0.041	0.010	0.043	0.043	0.298	0.044	0.044	0.232	0.046	0.046	0.303	0.047	0.047	0.476
10	0.035	0.035	0.098	0.038	0.038	0.030	0.040	0.040	0.091	0.041	0.041	0.017	0.043	0.043	0.292	0.044	0.044	0.257
15	0.031	0.031	0.038	0.034	0.034	0.048	0.036	0.036	0.108	0.037	0.038	0.189	0.039	0.039	0.184	0.041	0.041	0.246

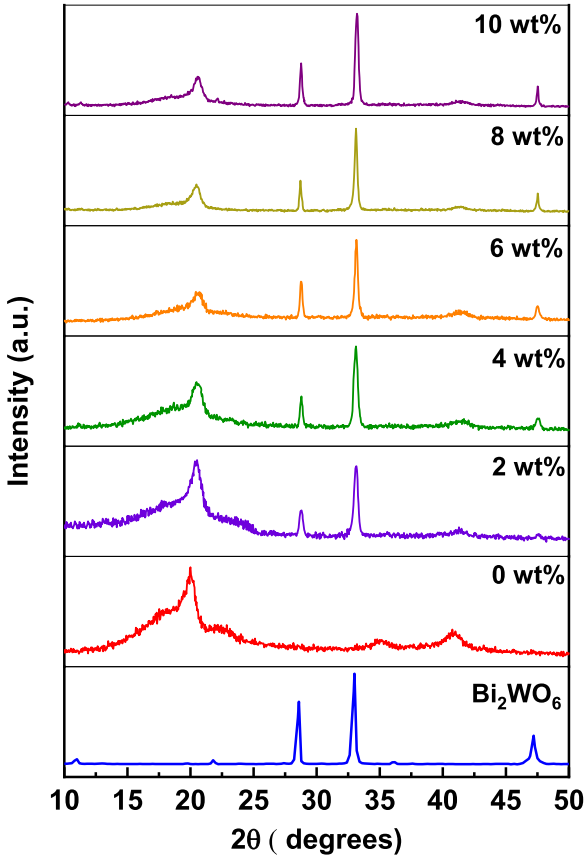

Fig. 2

The XRD patterns of Bi_2WO_6, P(VDF-TrFE), and P(VDF-TrFE)–Bi_2WO_6 nanocomposites at different wt% of Bi_2WO_6.

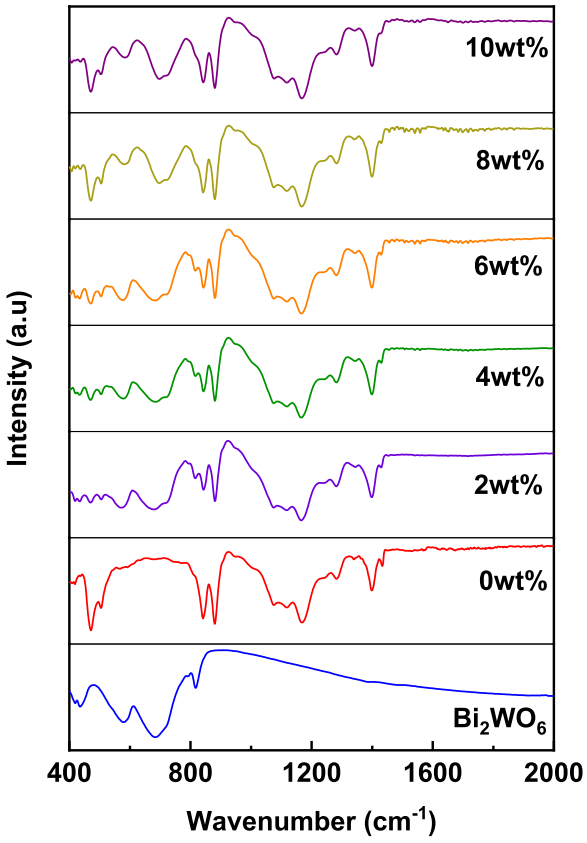

Fig. 3

The FTIR spectrum of Bi_2WO_6, P(VDF-TrFE), and its nanocomposites at different Bi_2WO_6 wt%.

$$RPE\ (\%) = \left(1 - \frac{N}{N_0}\right) \times\ 100\% \tag{17}$$

3 Results and discussions

3.1 Structural and morphological of P(VDF-TrFE)–Bi_2WO_6 nanocomposites

3.1.1 Crystalline structure

Fig. 2 shows the XRD patterns of Bi_2WO_6, P(VDF-TrFE), and P(VDF-TrFE)-Bi_2WO_6 nanocomposites. The Bi_2WO_6 shows its characteristic diffraction peaks. These peaks match the known orthorhombic structure of Bi_2WO_6 (JCPDS card No. 01-079-2381). The strong reflections appear around 10.7°,28.7°, 28.5° and 32.9°, 48°, 55.9°, 58.6°, 76° and 87.3° 2θ corresponding to (020), (131), (200), (202), (133), (262), (333), and (204) Bi_2WO_6 lattice planes respectively. This confirms the formation of crystalline Bi_2WO_6 with no other phases present.

On the other hand, the P(VDF-TrFE) XRD pattern shows the expected nature of semicrystalline copolymer peaks. In particular, the peak appears near 20° 2θ, corresponding to the (110)/(200) planes of the ferroelectric β-phase of P(VDF-TrFE) [43–45]. The peaks observed around 35° and 40° 2θ are typically higher order reflections of the β-phase crystalline structure. These peaks confirm the copolymer semicrystalline of P(VDF-TrFE). The XRD patterns of P(VDF-TrFE)-Bi_2WO_6 nanocomposites with different wt% ranging from 2 to 10 wt% of Bi_2WO_6 nanosheets show all the peaks of both components. As the Bi_2WO_6 content increases, the intensity of the Bi_2WO_6 peaks grows stronger relative to the P(VDF-TrFE) peaks, but both sets remain clearly present. No new peaks appear and the existing peaks do not shift. For example, the polymer peak at ≈20° is still visible in all composites, and new peaks at higher angles (from Bi_2WO_6) emerge just as expected. This is similar to other similar composites of P(VDF-TrFE)-based composites, where one sees the P(VDF-TrFE) β-peak near 20° 2θ plus distinct peaks of the added ceramics [46–48]. Because the composite patterns are just the sum of the two individual patterns, this confirms that there is no chemical reaction or new phase formed between P(VDF-TrFE) and Bi_2WO_6. Each phase retains its original crystal structure. The XRD thus confirms the stability of both Bi_2WO_6 and P(VDF-TrFE) after mixing. The P(VDF-TrFE) and Bi_2WO_6 coexist without altering each other's lattice.

3.1.2 FTIR analysis

Further analysis of the structure of P(VDF-TrFE) copolymer and its nanocomposites was conducted using FTIR. Fig. 3 shows the FTIR spectrum of P(VDF-TrFE), Bi_2WO_6, and P(VDF-TrFE)-Bi_2WO_6 nanocomposites. The Bi_2WO_6. For Bi_2WO_6, the main absorptions appear in the low-wavenumber region, between 420 cm^{-1} and 440 cm^{-1}, and match the expected Bi–O vibrations. On the other hand, the absorption peaks at around 580, 680, 720, and 819 cm^{-1} in the

spectrum of pure Bi_2WO_6 are attributed to the symmetric W-O stretch/Bi-O stretch, stretching W-O-W, and stretching O-W-OH, respectively, which are common for Bi_2WO_6 [49–51].

For pure P(VDF-TrFE), the spectrum shows the typical characteristic bands of PVDF-based ferroelectric polymers. The β-phase markers are commonly observed at 840, 880, 1070, 1230, and 1401 cm-¹. These bands are widely used to confirm the polar phase in P(VDF-TrFE). On the other hand, a weaker contribution near 735 cm^{-1} and 1119 cm^{-1} is often referred to as α-phase [43–45].

The FTIR spectra of the nanocomposite with Bi_2WO_6 content ranging from 2 wt% to 10 wt% show that all characteristic peaks of P(VDF-TrFE) and Bi_2WO_6 are present together. The polymer bands remain at the same positions, and the Bi_2WO_6 metal–oxygen bands remain visible in the same low wavenumber region, typically becoming more pronounced as the filler loading increases. No new peaks, the FTIR spectra of P(VDF-TrFE)-Bi_2WO_6 nanocomposites cover all characteristic peaks in both P(VDF-TrFE) and Bi_2WO_6 phases. This supports that the P(VDF-TrFE)-Bi_2WO_6 nanocomposites maintain the original structures of both components, consistent with the XRD results, and it indicates high chemical stability with mixing dominated by physical incorporation rather than new bond formation [46,47].

3.1.3 The microstructure analysis

The microstructure of P(VDF-TrFE) and its composites was conducted using SEM. Fig. 4 shows the SEM of Bi_2WO_6, P(VDF-TrFE), and P(VDF-TrFE)-Bi_2WO_6 nanocomposites at different wt%. The Bi_2WO_6 Fig. 4(a) shows a plate-like structure with an average length of about 4 μm and a thickness of about 130 nm, consistent with the well-known tendency of layered Aurivillius-type titanates to form high-aspect-ratio platelets, which can promote strong interfacial contact and effective stress transfer when embedded in polymers. The P(VDF-TrFE) morphology exhibits a smooth surface without any obvious morphology. For the composites Fig. 4(b-f), introducing Bi_2WO_6 progressively increases surface roughness and the number of visible platelet edges, while maintaining generally good dispersion up to 8 wt%. At a low concentration, i.e., 2 wt% Fig. 4(b), the Bi_2WO_6 sheets are well disposed within the P(VDF-TrFE), suggesting efficient incorporation into the matrix. Further increases in Bi_2WO_6 content to 4 wt% Fig. 4(c) and 6 wt% Fig. 4(d), the platelets become more apparent and more uniformly distributed, indicating that the processing route can accommodate higher ceramic loadings while largely preventing restacking of the sheets. At high Bi_2WO_6 content, such as 8 wt% Fig. 4(e), the microstructure typically shows a denser distribution of platelets with occasional local proximity between neighboring sheets, which is expected as inter-particle spacing decreases with loading. At 10 wt% Fig. 4(f), slight agglomeration becomes noticeable, possibly because there are more interactions between particles and the matrix is less mobile when there is more filler, which can lead to partial restacking or cluster formation in plate like fillers with a high aspect ratio.

In addition to filler loading, the surface state and morphology of Bi_2WO_6 nanosheets may additionally affect the composite response. In metal oxides, oxygen vacancies and related surface defects are electronically active and can modify local electronic characteristics and trapped-charge behavior; in Bi_2WO_6 specifically, oxygen-vacancy conditions have also been shown to affect phase equilibrium and surface morphology. Previous studies additionally show that morphology, size-related structural control, and interfacial area in PVDF- and P(VDF-TrFE)-based systems can strongly influence functional behavior, while ceramic incorporation can alter wettability, porosity, and matrix–filler interactions [52,53].

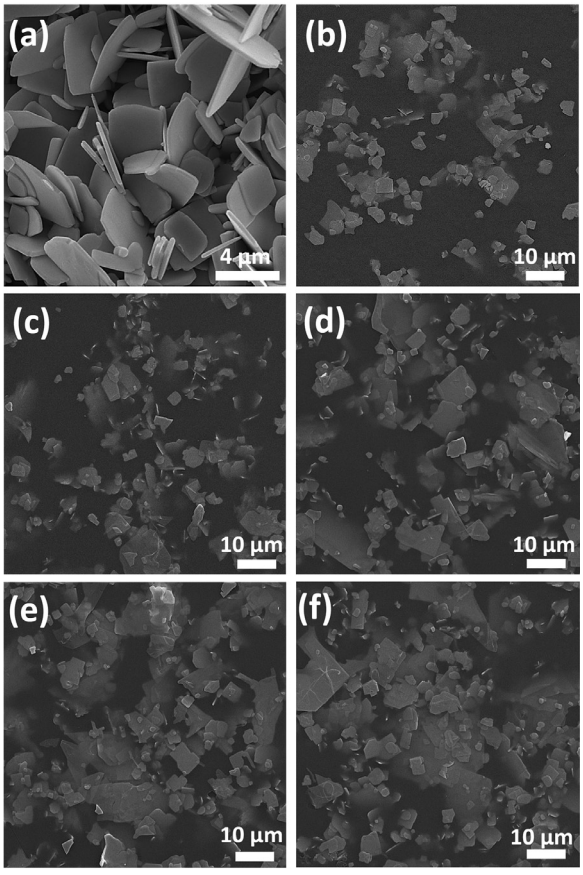

Fig. 4

SEM micrographs of (a) Bi_2WO_6, (b) P(VDF–TrFE)-Bi_2WO_6 nanocomposites containing 2 wt%, (c) 4 wt%, (d) 6 wt%, (e) 8 wt%, and (f) 10 wt%.

It should be noted that in this work, the maximum loading of Bi_2WO_6 sheet was limited to 10 wt% to reach a practical optimum between shielding performance and composite structural stability. High filler fractions are commonly used in conventional polymer shields, nanosheet fillers tend to agglomerate at high concentrations, which can lead to interfacial defects and reduced mechanical compliance. In the present system, Bi_2WO_6 nanosheets were well dispersed up to 10 wt% but higher loading quantities showed the severity of agglomeration in the microstructure. Moreover, P(VDF-TrFE) is a relatively dense fluoropolymer, and Bi_2WO_6 is a heavy oxide filler, thus an efficient attenuation may be obtained at moderate loading without sacrificing flexibility. The maximum Bi_2WO_6 loading was restricted to 10 wt% to provide a feasible trade-off between shielding performance and composite integrity. While higher filler fractions are usually employed for conventional polymer shields,

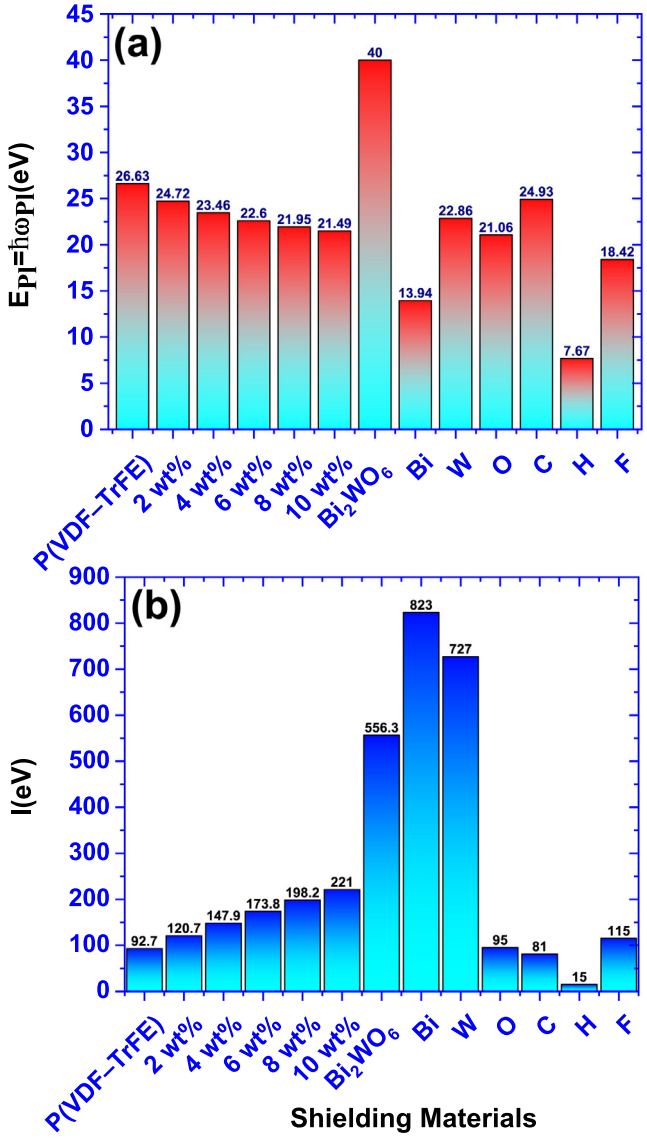

Fig. 5

(a) Bulk plasmon energy, and (b) mean excitation energy I(eV) for synthesized shielding P(VDF-TrFE)-Bi_2WO_6, with $0 \leq$ wt% < 100, in comparison to the pure elements of their components.

2D fillers are more prone to agglomeration at high contents, which could result within interfacial flaws and influence mechanical compliance. In our system, Bi_2WO_6 nanosheets remained well dispersed up to 10 wt% as shown in Fig. 4(f).

3.2 Bulk plasmon and mean excitation energy of the stopping medium

The E_{Pl} and I are the two key parameters that govern the electronic stopping cross-section values and thus rationalize the simulation trends across dielectric composition. Fig. 5 shows the computations of bulk plasmon energy $E_{Pl}= \hbar\omega_{Pl}$ and mean excitation energy I(eV) for fabricated shielding nanocomposites beside the individual elements of their components. The bulk plasmon energy for the synthesized shielding materials was calculated according to the following formalism [54]

$$E_{Pl} = 28.816\sqrt{\rho \sum_i \frac{Z_i}{A_i}} \tag{18}$$

Where ρ is density(gm/cm^3), Z_i /A_i is the ratio of the effective atomic number to the effective molecular weight of element i in the composite sample. The plasmon energy corresponds to a collective oscillation associated with wave-like excitation (a free-electron gas) of valence electrons in the matter. For advanced particle-stopping models based on the dielectric function formalism, the total electronic energy loss is the sum of energy lost to collective excitations (plasmons) involving valence electrons and to individual excitations due to ionizing core electrons. High-E_{Pl} medium indicates a denser valence-electron gas, which contributes to the material's ability to slow ions. The mixing of organic polymers P(VDF-TrFE) with inorganic ceramics Bi_2WO_6 generates a heterogeneous electronic structure environment. The P(VDF-TrFE) polymer contains both C–H and C–F bonds, which give it distinctive properties. In Fig. 5a, the plasmon energy for pure polymer P(VDF-TrFE) is 26.63 eV and 40 eV for pure Bi_2WO_6 filler, because the P(VDF-TrFE) and Bi_2WO_6 both have more valence electron densities, allowing higher plasmon energy values compared with pure element or nanocomposite samples. While in the nanocomposite samples (wt%=2–10), the plasmon value drops steadily from 24.7 eV to 21.49 eV, because the replacement of organic polymers P(VDF-TrFE) with inorganic ceramics Bi_2WO_6 leads to a reduction in the number of delocalized electrons (i.e., decrease in plasmon-active electron density), which can contribute to plasmon fluctuations, despite raising bulk density of the samples.

Fig. 5b depicts the mean excitation energy I(eV), which was calculated using the convolution approximation in CasP software [55], for synthesized shielding composites alongside the individual elements of their components. The I(eV) values vary tremendously from 97.87 eV (for pure copolymer,0wt%) to 823 eV (for pure ceramic, 100wt%). This is the predicted behavior according to Bragg's additivity rule because the I(eV) value of a nanocomposite is the weighted average of the I(eV) values of its individual elements. The P(VDF-TrFE) polymer is composed of lower Z materials (H, C, F) showing low I(eV) values of about 15, 81, and 115 eV, respectively. But the filler ceramic includes higher-Z materials, W and Bi, which produce exceedingly large I(eV) values of about 727 and 823 eV, respectively. The composite materials have wide polymer-oxide interfaces. These regions can alter local fields and introduce additional polarization processes that contribute to electronic energy dissipation.

3.3 Analysis of Bragg additivity rule for proton and Li in P(VDF-TrFE)- Bi_2WO_6 composites

The electronic stopping power S_e and PR for proton and lithium ions striking on P(VDF-TrFE) with ceramic weight fractions ranging from wt%=0 to 100 have been figured out at different ranges of projectile energies (1eV-100 MeV), via the SRIM program version 2013. To our best knowledge, no S_e and PR data is available for the nanocomposite. Therefore, the central guide for predicting S_e and PR for the composite will rely on SRIM program computations, based on the validity of the Bragg rule and on

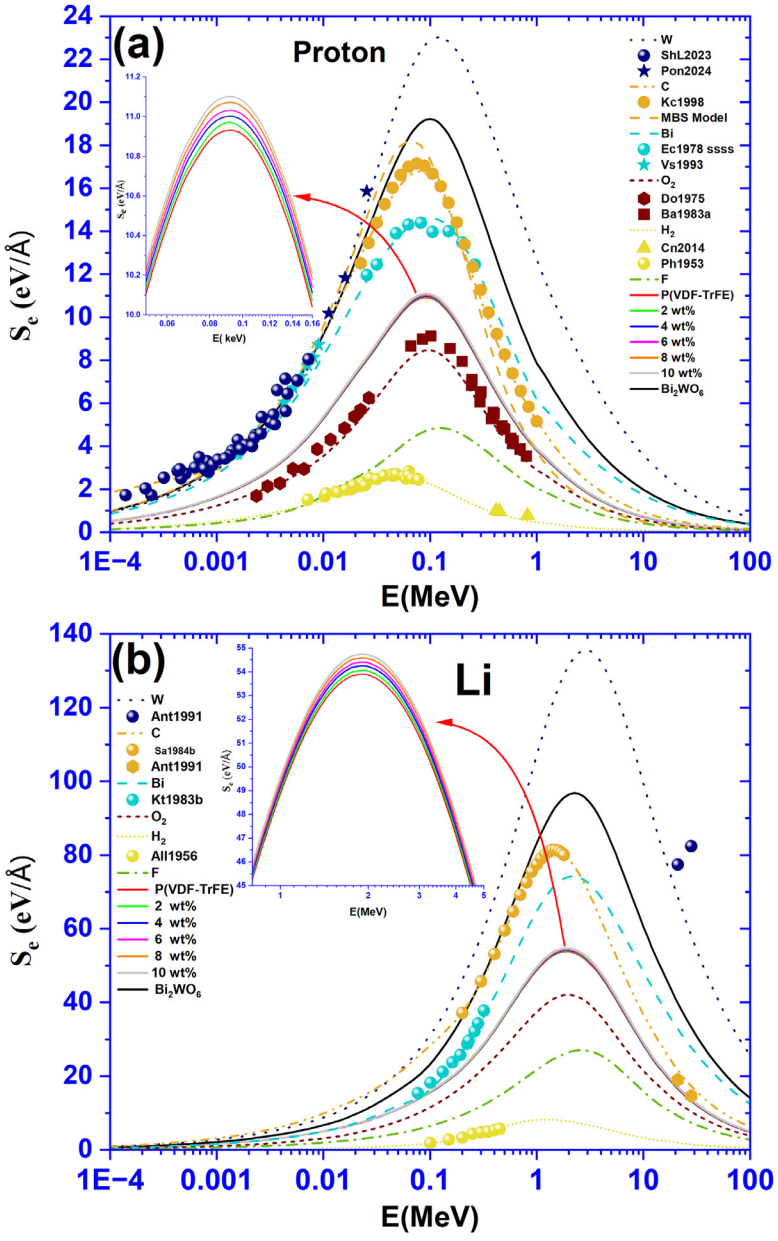

Fig. 6

Electronic linear stopping power for (a) proton and (b) lithium ions via P(VDF-TrFE)-Bi_2WO_6, ($0 \leq$ wt% ≤ 100) as a function of projectile energy. The SRIM computations for fabricated shields (pure individual elements) are compared with experimental results for pure solid targets (Symbols).

preceding experimental work for all individual elements in the nanocomposite's composition. In this study, the International Atomic Energy Agency (IAEA) literature labeling norms were adhered to in all figures throughout this work. Fig. 6(a,b) represents a comparison of the electronic S_e for proton and Li ions in P(VDF-TrFE)-Bi_2WO_6 shields, (where $0 \leq$wt%$\leq$ 100) versus experimental measurements for the pure solid (C, H_2, F, Bi, W, and O_2) and SRIM simulations, which utilize Bragg's rule to evaluate energy loss in composite target. Fig. 6(a) represents slight variance between the SRIM computations and experimental values for proton transferring in Bi (Ec1978) [56] and (Vs1993) [57], W(ShL2023) [58] and (Pon2024) [59], O_2(Do1975) [60] and (Ba1983a) [61], C(Kc1998) [62], H_2 (Ph1953) [63] and (Cn2014) [64]. It is worth mentioning that the carbon stopping derived from the MBS model dielectric formalism [65], along with optical ELF data [66] in the framework of the stopping power relation [67] is also compatible with the experimental measurements obtained by ion-backscattering analysis (Kc1998) [62] and SRIM computations using the Bethe-Bloch relation [68]. In Fig. 6(b), the Se of lithium has been plotted under the same conditions as in Fig. 6(a). It is observed that there is a good consistency between the SRIM results and experimental analysis for lithium moving in Bi (Kt1983b) [69], W(Ant1991) [70], O_2(An1978) [71], C(Sa1984b) [72], and (Ant1991) [70] and H_2 (All1956) [73]. These computations illustrate good reliability across pure materials to confirm the accuracy of SRIM predictions for individual elements

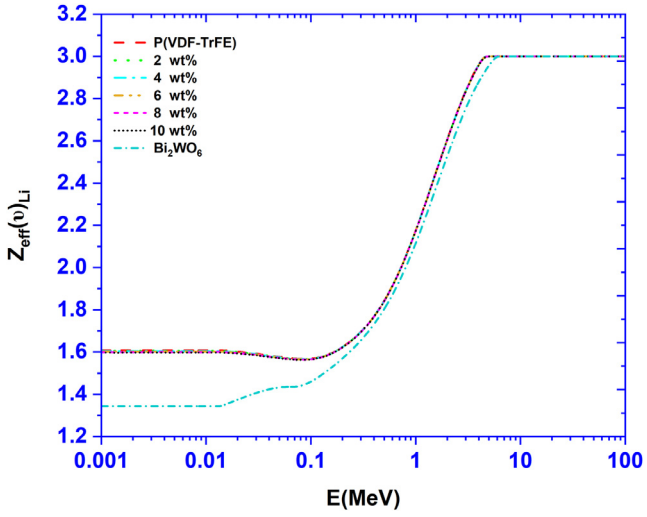

Fig. 7

Lithium effective charge versus energy estimated from the SRIM software for several fabricated shield materials.

included in nanocomposite materials, to get the best estimations for Bragg rule additivity. Evidently, the Bragg peak position is around 100 keV for the proton and 2 MeV for the Li, where linear electronic stopping S_e(eV/Å) per atom is highest, because it depends mainly on the mass and charge of the projectile, not the nanocomposite composition. In the nanocomposite series, the Se data are found to increase systematically with the Bi_2WO_6 wt fraction, from 0 wt% to 10 wt%. The polymer matrix phase remains relatively dominant in the microstructure and regulates the effective stopping response. That's because tungsten and bismuth (high atomic numbers) have substantially higher S_e than lighter elements such as carbon, hydrogen, fluorine, and oxygen. Therefore, a higher weight fraction of Bi_2WO_6 atoms leads to an improvement in the mean excitation energy of the nanocomposite, which elevates the energy loss by swift ions as expected from Fig. 6(b).

3.4 Effective charge analysis of lithium ions

In inelastic collisions, when charged particles travel through a medium, they lose energy primarily via electronic stopping, exciting or ionizing atomic electrons along their trajectories. Fig. 7 displays the velocity-dependent effective charge of Li ions versus kinetic energy up to 100MeV in P(VDF-TrFE)-Bi_2WO_6 shields for ($0\leq$ wt% $\leq$100), as carried out from SRIM software electronic stopping power computations. The effective charge ratio $Z_{eff}\ (\upsilon)_{Li}\ /Z_{eff}\ (\upsilon)_p$ mainly relies on projectile velocity, which controls the rate of ionization and electron capture influenced by the penetrating ion. Notwithstanding the noticeable differences in chemical composition formula, density of samples, and electronic structure between the polymer-rich and oxide-rich extremes, all curves show S-shaped behavior. This behavior of the projectile resolves into three distinct regimes: (i) a low projectile velocity plateau, (ii) a semi-straight transition region distinguished by quickly rising projectile velocity, and (iii) a high-velocity saturation related to complete stripping of the projectile.

At the lower specific energy region ($E \leq 10^{-2}$MeV), the effective charge of Li stays relatively constant in the range $Z_{eff}\ (\upsilon)_{Li} \approx$1.4–1.57, independent of the Bi_2WO_6 fraction. In this region, Li ions undergo substantial electron capture from the composite medium, attenuating their effective charge and resulting in a slightly lower effective charge with increasing ceramic fraction wt%. Generally, the charge exchange occurs strongly when the projectile's speed is lower than the Bohr velocity ($\upsilon \leq \upsilon_{Bohr}$), which corresponds to proton energy of about 25 keV and for Li about 175 keV. A slight systematic downward shift of the pure Bi_2WO_6 curve in the lower ion-energy region suggests a higher stopping density and stronger electronic localization. However, these differences diminish swiftly as energy increases, indicating that compositional effects act mainly through charge exchange at low ion velocities rather than through any modification of the stripping dynamics at high ion velocities.

In the intermediate-energy region ($10^{-2} \leq E \leq 0.72$MeV), the effective charge increases monotonically with projectile velocity, approaching the full-charge limit at higher energy due to velocity-driven stripping and universal charge buildup. One can see the effective charge for the Li projectile rise from 1.6 to 1.97 and is almost independent of the volume fraction between 0 wt% and 10 wt% of the composite, leading to overlapping curves. From the same perspective, when the projectile velocity surpasses the adiabatic response time of atomic-bound electrons, the electron capture process becomes gradually suppressed, while direct ionization and ejected electrons dominate. The close overlap of the curves for various Bi_2WO_6 wt fraction values in this region is an important outcome. It reveals that beyond a high enough projectile velocity, the effective charge value becomes a necessary kinematic quantity that is found mainly by the dynamics of the projectile rather than the target chemical composition. Furthermore, this region has the highest sensitivity of the electronic stopping power to Li-ion velocity. This has direct consequences for radiation damage, energy deposition profiles, and ion-beam modification in nanocomposite materials.

For high-energy, the projectile energies exceed approximately 1 (MeV), the mean effective charge plateaus at Z_{Li}=3, throughout fabricated shielding nanocomposites, compatible with saturation at the full strip of a lithium projectile. Within this maximum velocity range, the projectile velocity significantly exceeds the characteristic electronic velocities of the target material, thereby suppressing electron-capture processes and shifting the charge-state distribution toward bare-ion behavior. Consequently, the ion can be regarded as a point charge (unscreened coulomb center), and the electronic stopping power is proportional to $(Z_{eff})^2/\beta^2$. This statement reinforces the physical condition that the effective charge cannot exceed the ionic nuclear charge, Z_{Li}=3, and confirms the internal consistency of SRIM's calculations for nanocomposite materials.

3.5 Projected range of swift ions

The PR of protons and lithium ions moving in prepared nanocomposites, evaluated at a projectile energy of T = 100 MeV, is depicted in Fig. 8(a) and (b). At the same projectile energy, the proton's PR is larger than that of the Li ion in the same nanocomposite shield. Obviously, the (PR) of the projectiles was

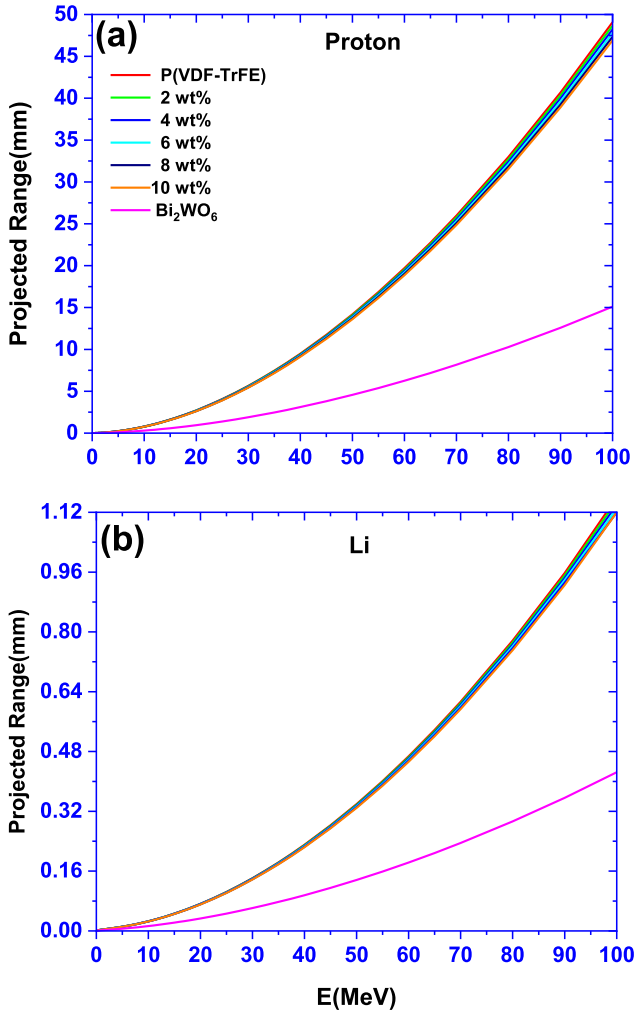

Fig. 8

Projected range created by (a) H and (b) Li ions moving in P(VDF-TrFE) -Bi_2WO_6 as a function of the energy with different ceramic fractions.

varying inversely to the density of the material at all projectiles' energies according to the projected range formula Eq. (4). The results suggests that there are significant differences for the seven nanocomposite shields, however as increasing wt%, the differences in the projected ranges for proton and Li projectiles begin to clear in the order PR(0wt%)>PR(2wt%)>PR(4wt%)>PR(6wt%)>PR(8wt%)>PR(10wt%)>PR(100wt%). Therefore, within the range of physical composition variation examined herein, the maximum amount of Bi_2WO_6, which is about 10 wt%, elevates the capacity of the 0.9 P(VDF-TrFE)/0.1Bi_2WO_6 to absorb protons or Li, because it has the highest stopping power, and large density among samples (0≤ wt% <10).

As shown in Fig. 9, the projected-range ratio $PR_H(\beta)$/ $PR_{Li}(\beta)$ stays bigger than unity over the examined velocity β range (0.112–0.126), asserting that protons move deeper than lithium ions when both penetrate the target with the same velocity. However, as the volume fraction of ceramic Bi_2WO_6 increases, heavy, highly charged ions increase energy loss in the denser composite (high-Z matrix). This reduction in the relative range ratio draws attention

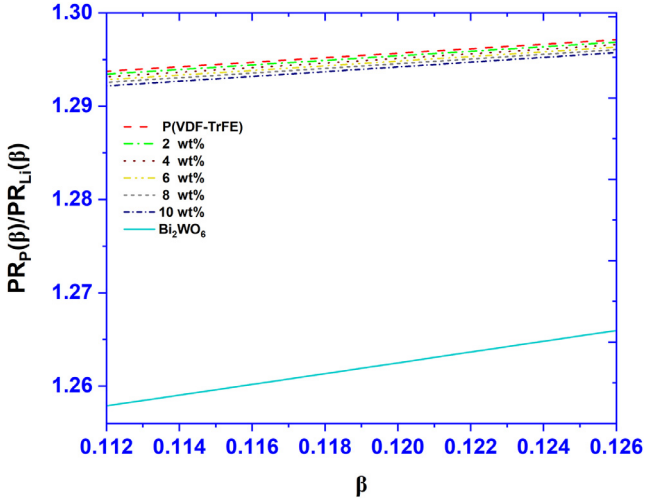

Fig. 9

Projected range ratio $PR_H(\beta)$/ $PR_{Li}(\beta)$ as a function of ion-energy crossing P(VDF-TrFE)-Bi_2WO_6.

to the fact that the PR_{Proton}/PR_{Li} is fine-sensitive to the atomic structure rather than to the mass fraction alone. The existence of bismuth and tungsten atoms in the structure of Bi_2WO_6 ceramic not only reinforces the total electronic density of the composite sample but also enhances elastic collision events that reduce the lithium path more efficiently than protons. Hence, the ratio PR_{Proton}/PR_{Li} facilitates an indirect index of the nanocomposite's effective electronic density.

3.6 Ionizing radiation shielding features

This work started by simulating the linear attenuation coefficient (μ) for all polymers prepared in using Geant4 Monte Carlo MC toolkit (μ_{sim}) across 0.015 MeV to 15 MeV. The results obtained from the Geant4 are then compared with those obtained from PhyX/PSD (μ_{theo}). Table 1 compiles μ_{sim} and μ_{theo} for all investigated compositions enabling a point-by-point comparison over both energy and compositions. The Geant4 values closely track the Phy-X references at most energies, with only isolated points showing noticeable deviations, as indicated by the Δ% columns. Overall, Δ% between both datasets is small, as reflected by the Δ% reported in Table 1. The average Δ% remains below 1% for all compositions with values of 0.209%, 0.216%, 0.266%, 0.430%, 0.566%, and 0.317% for 0 wt%, 2 wt%, 4 wt%, 6 wt%, 8 wt% and 10 wt% respectively, indicating a generally tight point-by-point agreement between the two datasets. In addition, the χ^2goodness-of-fit results (not shown) support this consistency yielding χ^2 values of 5.81×10^{-3}, 6.55×10^{-3}, 3.55×10^{-2}, 1.355, 4.347, and 3.59×10^{-2} for 0 wt%, 2 wt%, 4 wt%, 6 wt%, 8 wt% and 10 wt% respectively, with corresponding reduced χ^2 values of 2.42×10^{-4}, 2.73×10^{-4}, 1.48×10^{-3}, 5.65×10^{-2}, 0.181, and 1.50×10^{-3}. As a result, these statistics confirm that the Geant4 model reproduces the theoretical data obtained from Phy-X with high fidelity across the investigated energy range.

Fig. 10 shows a direct visual check for the Geant4 results against the Phy-X/PSD data by plotting μ as a function of photon energy for all compositions. Across all energy range, the two

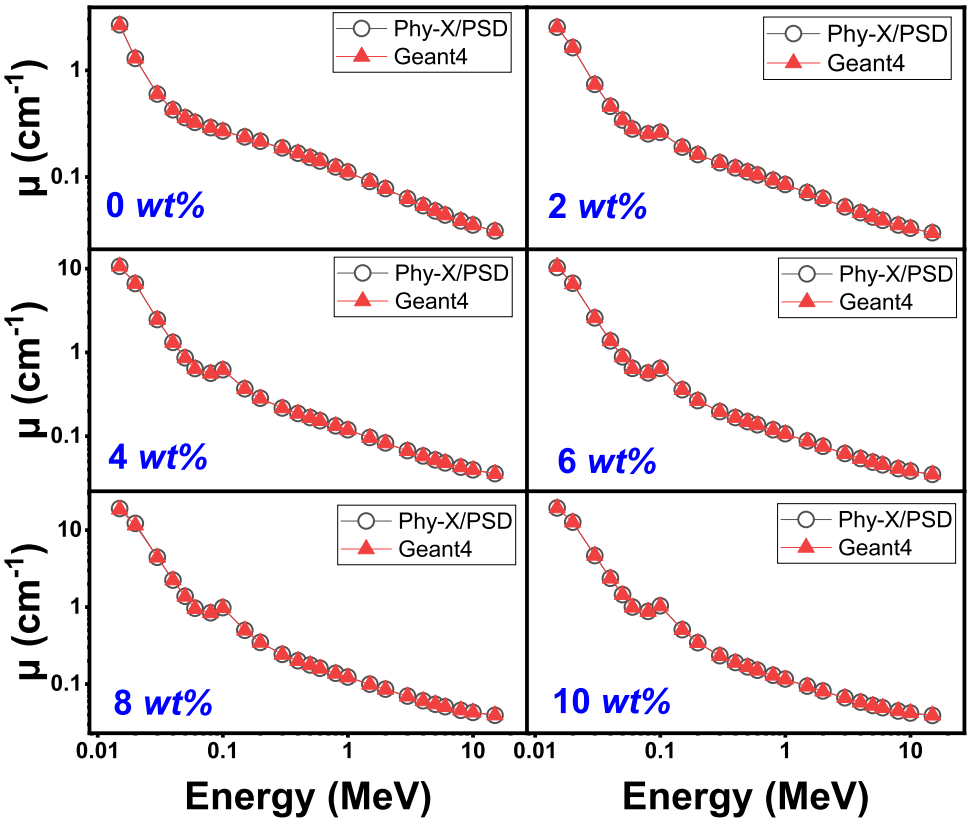

Fig. 10

μ as a function of photon energy for all compositions prepared in this work comparing Geant4 simulations with Phy-X/PSD theoretical data.

datasets essentially sit on top of each other in every panel, which is consistent with the small $\Delta\%$ values already reported in Table 1 and the low χ^2 statistics for most compositions. At the lowest energies, up to 0.1 MeV, μ drops very rapidly with increasing energy. This steep fall is the classical signature of photoelectric absorption, where the interaction probability decreases strongly with photon energy and increases strongly as well with atomic number (Z). The sudden spikes shown in some samples are the absorption K-edges for the heavy constituents such as bismuth (Bi) and tungsten (W) presented in the compositions. Moving into the intermediate energy range, up to 1 MeV, the decline in μ becomes noticeably more gradual due to Compton scattering which becomes the main contributor to attenuation. Finally, above 1.022 MeV, pair production begins to contribute and the curves converge.

Fig. 11 summarizes how much of the total attenuation is driven by Compton scattering by plotting the ration $R(\%) = \frac{\mu_{Compton}}{\mu_{total}} \times 100\%$ as a function of photon energy and samples used in this study. At low energies, below 0.1 MeV, R is small for all compositions (blue-green region), indicating that Compton scattering contributes to only minor fraction of μ_{total} because photoelectric effect dominates in this regime. For example, at 0.015 MeV, R is 10.67%, 4.29%, 2.66%, 1.92%, 1.49%, and 1.22% for 0 wt%, 2 wt%, 4 wt%, 6 wt%, 8 wt% and 10 wt% respectively. As energy increases, R rises rapidly and reaches a broad plateau (yellow-red), showing that Compton scattering

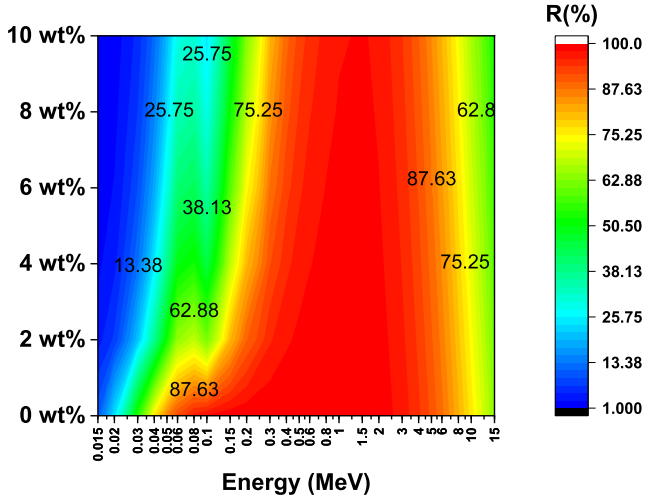

Fig. 11

Compton scattering contribution ratio, $R(\%) = \frac{\mu_{Compton}}{\mu_{total}} \times 100\%$, as a function of photon energy and filler loading (0–10 wt%).

becomes the main contributor over the intermediate energies. For instance, R becomes, at 0.8 MeV, 99.99%, 99.33%, 98.68%98.03%, 97.38%, and 96.74% for 0 wt%, 2 wt%, 4 wt%, 6 wt%, 8 wt% and 10 wt% respectively. This behavior is consistent with the well-known transition from photoelectric-dominated attenuation to

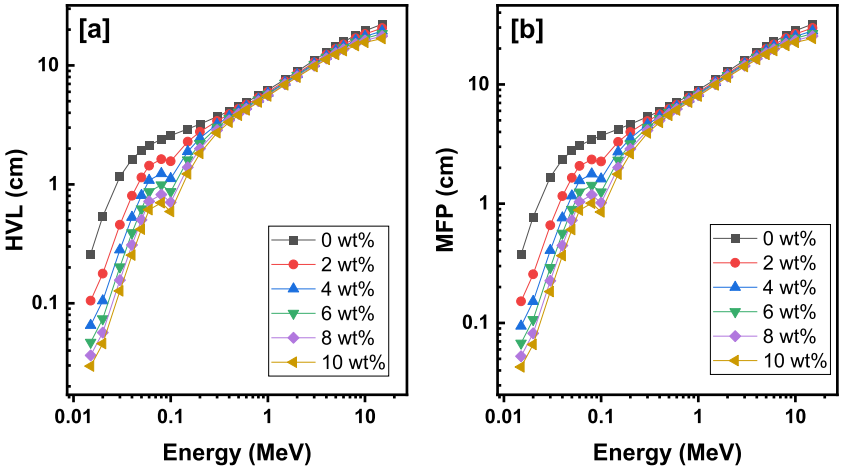

Fig. 12

(a) Half-value layer (HVL) and (b) mean free path (MFP) as a function of photon energy for all compositions (0–10 wt%).

Compton-dominated attenuation as photon energy increases. At even higher energy, 10 MeV, for example, *R* gradually decreases again to reach 76.07%, 73.96%, 71.95%, 70.04%, 68.21%, and 66.46% for 0 wt%, 2 wt%, 4 wt%, 6 wt%, 8 wt% and 10 wt% respectively. It is also observed that as Bi_2WO_6 content increases, *R* decreases as Compton-dominate region becoming less extensive at the lowest energies because the heavier constituents strengthen the photoelectric component.

Fig. 12 shows the (a) half-value layer (HVL) and (b) mean-free path (MFP) versus photon energy in the range of 0.015 MeV to 15 MeV for all prepared compositions. Both HVL and MFP increases with photon energy for all prepared compositions, reflecting the expected reduction of μ with energy. It is worth mentioning that the effect of adding Bi_2WO_6 is most evident in the low energy region, where adding more Bi_2WO_6 will systematically lowers both HVL and MFP, meaning that thinner samples are needed to attenuate low-energy photons when the composite contains a higher fraction of heavy constituents. Above 1 MeV, where Compton scattering dominates, the curves for all samples draw closer together, indicating that composition-driven differences in μ—and therefore in HVL/MFP—become less pronounced as energy increases.

Fig. 13 shows variation of the effective atomic number with photon energy on a log-log scale for all investigated compositions. Two clear trends stand out. First, Z_{eff} increases systematically with Bi_2WO_6 content, and the separation between curves is largest at low energies, where attenuation is most sensitive to high-Z constituents. This behavior is consistent with the photoelectric regime, in which interaction probability is strongly enhanced in higher-Z media and drops rapidly with increasing energy, so even modest changes in composition are reflected in Z_{eff}. For example, at 0.015 MeV, the value of Z_{eff} is 7.56, 16.11, 23.05, 28.80, 33.65, and 37.78 for 0 wt%, 2 wt%, 4 wt%, 6 wt%, 8 wt% and 10 wt% respectively. As energy increases to reach 1 MeV, the values drop to 5.50, 5.61, 5.71, 5.82, 5.94, and 6.06 respectively for 0 wt%, 2 wt%, 4 wt%, 6 wt%, 8 wt% and 10 wt% samples. Second, Zeff decreases sharply as energy rises into the hundreds-of-keV region and then approaches a relatively flat

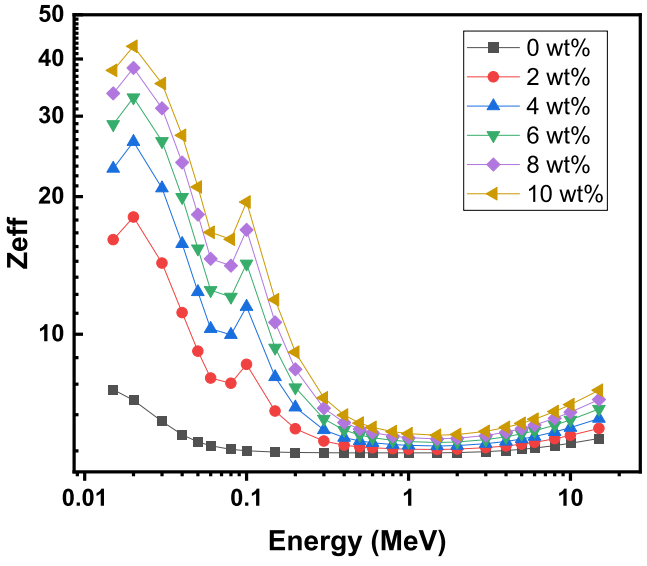

Fig. 13

Effective atomic number (Zeff) versus photon energy for all compositions (0–10 wt%).

minimum around the MeV range, which matches the transition to Compton-dominated attenuation where the dependence on Z is much weaker (more closely tied to electron density than to Z itself). At the highest energies, a slight upturn becomes noticeable for the filled samples, which is reasonable once pair production becomes energetically allowed above 1.022 MeV and begins to contribute more at higher energies, particularly in materials containing heavier elements. The oscillations observed at the low-energy can be linked to absorption K-edge effects of heavy constituents, which can introduce localized changes in effective interaction behavior when the photon energy crosses inner-shell binding thresholds.

Fig. 14 shows (a) the transmission factor (TF) and (b) radiation protection efficiency (RPE) for all prepared samples versus photon energy. For a fixed sample thickness, 0.5 cm for instance, TF

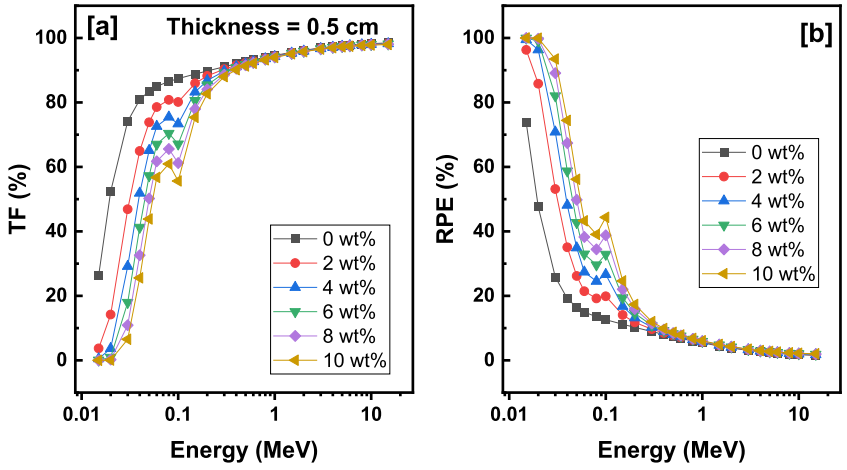

Fig. 14

(a) Transmission factor (TF) and (b) radiation protection efficiency (RPE) versus photon energy for all compositions (0–10 wt%) at a fixed sample thickness of 0.5 cm.

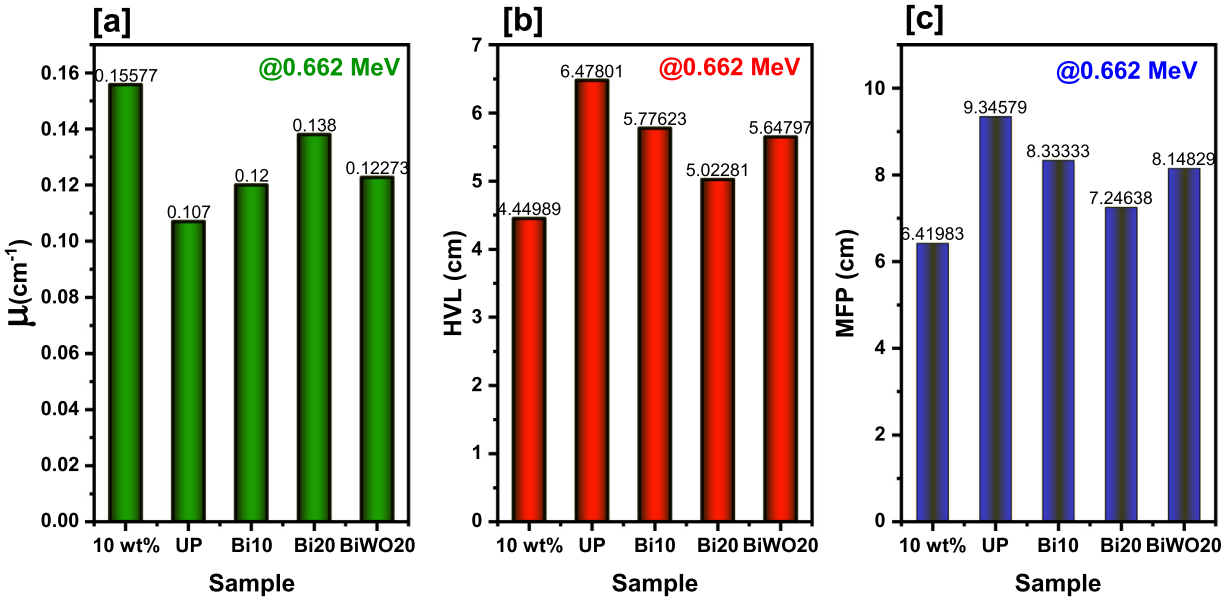

Fig. 15

Comparative shielding performance of the present 10 wt% P(VDF-TrFE)–Bi_2WO_6 nanocomposite and analogous polymer-based shielding materials at 0.662 MeV: (a) linear attenuation coefficient, μ; (b) half-value layer, HVL; and (c) mean free path, MFP.

increases steadily with energy for every sample, which simply reflects the well-known reduction in attenuation strength as photon energy rises. This means higher energy photons penetrate more readily, so a larger fraction is transmitted. Bi_2WO_6 content effect is most visible at the higher energies, where higher Bi_2WO_6 content leads to lower TF at a specific photon energy, indicating improved attenuation at the same thickness, with the highest Bi_2WO_6 content providing the lowest transmission. RPE, on the other hand, remains very high at low energies and then decreases gradually as energy increases, while higher Bi_2WO_6 content maintain higher RPE than the base material across the range. For example, at 0.015 MeV and 0.5 cm sample, the TF reaches 26.34%, in 0 wt%, while this value dropped to reach 3.71% in 2 wt% and almost zero for the rest of prepared samples. These values spikes when increasing the energy to 1 MeV and becomes ~94% in all samples. RPE, in contrast, reaches 73.66% in 0 wt% and ~100% in the rest of samples. As energy increases to 1 MeV, RPE declined to reach ~6% in all prepared samples.

In order to assess the real shielding effectiveness of the fabricated composites, the 10 wt% P(VDF-TrFE)–Bi_2WO_6 composite is compared to other polymer-based shielding materials at 0.662 MeV as illustrated in Fig. 15. The current composite is characterized by the largest value of linear attenuation coefficient, $\mu = 0.15577$ cm^{-1}, in comparison with UP, Bi10, Bi20 [74], and BiWO20 [75] composites, which have $\mu = 0.107$, 0.120, 0.138, and 0.12273 cm^{-1}, respectively. Moreover, the 10 wt% P(VDF-TrFE)–Bi_2WO_6 composite possesses the smallest HVL and MFP values, being 4.44989 cm and 6.41983 cm, respectively. The

above facts prove that the P(VDF-TrFE)-based nanocomposite with Bi_2WO_6 requires less shielding thickness and photon travel distance in comparison with those materials obtained from the literature.

4 Conclusion

The present study focuses on the fabrication of P(VDF TrFE)–Bi_2WO_6 nanocomposites. The combined XRD and FTIR results confirm the expected crystalline and vibrational properties of the combined structure and confirm the chemical stability of each phase after incorporation, while the microstructural observations demonstrate the well-dispersion of Bi_2WO_6 nanosheets in the P(VDF TrFE) host. The contribution of a dense, heavy oxide can reduce the electron density per unit mass because the effective ratio (Z/A) decreases more rapidly than the bulk density ρ increases; therefore, E_{PI} decreases. The I-values are strongly dependent on the E_{PI}, as collective electron density oscillations develop into a considerable trend of energy loss. The I-values increase with increasing Bi_2WO_6 fraction leading to a reduction in the Bethe-Bloch logarithmic term in the stopping formula. In contrast, variations in E_{PI} value modify the density effect (polarization screening) at greater projectile energy. These findings indicate that the addition of heavy-oxide fillers to the polymer matrix increased the electronic stopping power and reduced the projected range of protons and 3Li ions in the nanocomposite. Geant4 MC toolkit reproduced Phy-X/PSD attenuation coefficient (μ) over 0.015–15 MeV with consistently small deviations (average $\overline{\Delta\%}$ = 0.209–0.566%) and strong goodness-of-fit ($\chi^2 = 5.81 \times 10^{-5}$–$4.35 \times 10^{-2}$. Bi_2WO_6 addition systematically increased μ and improved thickness metrics at clinically/industrially relevant energies. For example, at 0.5 MeV, μ rose from 0.15255 to 0.18123 cm^{-1} while HVL fell from 4.54 to 3.82 cm and MFP from 6.56 to 5.52 cm from 0 to 10 wt%. The same compositional effect is reflected in Zeff, which increased strongly at low energy. Compton scattering dominated the mid-energy regime (R ≈ 96.74–99.99% at 0.8 MeV), while its share was much smaller at 0.015 MeV (R = 1.22–10.67%) and decreased again at higher energies (R = 66.46–76.07% at 10 MeV). Overall, the 10 wt% formulation provided the strongest attenuation among the tested composites across the spectrum, with the clearest advantage at lower energies where composition-driven differences are largest.

Declaration of competing interest

The authors declare that they have no known competing financial interests or personal relationships that could have appeared to influence the work reported in this paper.

Data availability

Data will be made available on request.

CRediT authorship contribution statement

Nabil Janan Al-Bahnam: Writing – original draft, Investigation. **Rahman I. Mahdi:** Writing – original draft, Methodology. **M.Kh. Hamad:** Writing – original draft, Investigation. **M.I. Sayyed:** Writing – review & editing, Investigation. **Yasser Maghrbi:** Writing – original draft, Methodology. **Kawa M. Kaky:** Writing – original draft, Investigation.

References

[1] M.N. Azman, N.J. Abualroos, K.A. Yaacob, R. Zainon, Feasibility of nanomaterial tungsten carbide as lead-free nanomaterial-based radiation shielding, Radiat. Phys. Chem. 202 (2023) 110492.

[2] M.K. Hamad, Effect of WO3 on structural, optical, mechanical, and ionizing radiation shielding properties of borate-tellurite glass network, Ceram. Int. 51 (8) (2025) 9763–9771.

[3] M.K. Hamad, Enhancing ionizing radiation shielding properties with PbO and ZnO substitutions in B2O3–BaO–TiO2 novel glass system, Radiat. Phys. Chem. 229 (2025) 112499.

[4] S. Kim, Y. Ahn, S.H. Song, D. Lee, Tungsten nanoparticle anchoring on boron nitride nanosheet-based polymer nanocomposites for complex radiation shielding, Compos. Sci. Technol. 221 (2022) 109353.

[5] N. Şahin, M. Bozkurt, Y. Karabul, M. Kılıç, Z.G. Özdemir, Low cost radiation shielding material for low energy radiation applications: epoxy/Yahyali Stone composites, Prog. Nucl. Energy 135 (2021) 103703.

[6] M.T. Alabsy, J.S. Alzahrani, M.I. Sayyed, D.I. Tishkevich, M.I. Abbas, A.M. El-Khatib, M. Elsafi, Gamma-ray attenuation and exposure buildup factor of novel polymers in shielding using Geant4 simulation, Materials 14 (2021) 5051.

[7] H. Zhang, F. Zhao, Y. Niu, Y. Yang, X. Feng, Z. Yuan, … S. Liao, Robust, puncture-resistant and self-healable composite rubber film shielding for gamma-rays via new interface design using inverse vulcanized polysulfide, React. Funct. Polym. 218 (2025) 106536.

[8] R.A. Surmenev, R.V. Chernozem, I.O. Pariy, M.A. Surmeneva, A review on piezo-and pyroelectric responses of flexible nano-and micropatterned polymer surfaces for biomedical sensing and energy harvesting applications, Nano Energy 79 (2021) 105442.

[9] P. Martins, A.C. Lopes, S. Lanceros-Mendez, Electroactive phases of poly (vinylidene fluoride): determination, processing and applications, Prog. Polym. Sci. 39 (4) (2014) 683–706.

[10] W.C. Yu, T. Wang, G.Q. Zhang, Z.G. Wang, H.M. Yin, D.X. Yan, … Z.M. Li, Largely enhanced mechanical property of segregated carbon nanotube/poly (vinylidene fluoride) composites with high electromagnetic interference shielding performance, Compos. Sci. Technol. 167 (2018) 260–267.

[11] G. Schiwietz, K. Czerski, M. Roth, F. Staufenbiel, P.L. Grande, Femtosecond dynamics–snapshots of the early ion-track evolution, Nucl. Instrum. Methods Phys. Res. B: Beam Interact. Mater. At. 225 (1–2) (2004) 4–26.

[12] J.F. Ziegler, M.D. Ziegler, J.P. Biersack, SRIM–The stopping and range of ions in matter (2010), Nucl. Instrum. Methods Phys. Res. B: Beam Interact. Mater. At. 268 (11–12) (2010) 1818–1823.

[13] R.I. Mahdi, K.A. Mahmoud, N.J. Al-Bahnam, M.I. Sayyed, K.M. Kaky, U. Altimari, Engineered composition and morphology: unveiling 2D bi_2 (W_{1-x}Mox) O_6 nanosheets for enhanced optical and ionizing protection applications, Mater. Today Commun. 45 (2025) 112415.

[14] A.L.F. De Barros, C. Mejia, D.V. Doreste, A. Domaracka, P. Boduch, H. Rothard, E.F. Da Silveira, Evaluation of the degradation cross-cection as stopping power dependence for pure and mixture molecular samples at cryogenic temperatures, Nucl. Instrum. Methods Phys. Res. B: Beam Interact. Mater. At. 570 (2026) 165926.

[15] N.E. Koval, F. Da Pieve, E. Artacho, Ab initio electronic stopping power for protons in Ga0. 5In0. 5P/GaAs/Ge triple-junction solar cells for space applications, R. Soc. Open Sci. 7 (11) (2020) 200925.

[16] P.H. Yannakopoulos, A.P. Skountzos, M. Vesely, Influence of ionizing radiation in electronic and optoelectronic properties of III–V semiconductor compounds, Microelectronics J. 39 (5) (2008) 732–736.

[17] S.T. Lau, K.Y. Leung, H.L.W. Chan, C.L. Choy, B. Sundaravel, I. Wilson, Effects of proton irradiation on the structure and properties of poly (vinylidene fluoride-trifluoroethylene) 80/20 mol.% copolymer, Ferroelectrics 273 (1) (2002) 9–14.

[18] M. Sharma, A. Gaur, J.K. Quamara, Swift heavy ions irradiated PVDF/BaTiO3 film as a separator for supercapacitors, Solid. State Ion. 352 (2020) 115342.

[19] N.N. Azman, S.A. Siddiqui, I.M. Low, Characterisation of micro-sized and nano-sized tungsten oxide-epoxy composites for radiation shielding of diagnostic X-rays, Mater. Sci. Eng., C 33 (8) (2013) 4952–4957.

[20] R.M. El-Sharkawy, Kh.S. Shaaban, R. Elsaman, E.A. Allam, A. El-Taher, M.E. Mahmoud, Investigation of mechanical and radiation shielding characteristics of novel glass systems with the composition xNiO-20ZnO-60B2O3-(20-x) CdO based on nanometal oxides, J. Non Cryst. Solids 528 (2020) 119754.

[21] G.A.M. Amin, M.H. Abd-El Salam, Optical, dielectric and electrical properties of PVA doped with Sn nanoparticles, Mater. Res. Express 1 (2) (2014) 025024.

[22] O.M. Hemeda, M.E.A. Eid, T. Sharshar, H.M. Ellabany, A.M.A. Henaish, Synthesis of nanometer-sized PbZrxTi1-xO3 for gamma-ray attenuation, J. Phys. Chem. Solids 148 (2021) 109688.

[23] H. Alavian, H. Tavakoli-Anbaran, Study on gamma shielding polymer composites reinforced with different sizes and proportions of tungsten particles using MCNP code, Prog. Nucl. Energy 115 (2019) 91–98.

[24] M.E. Mahmoud, R.M. El-Sharkawy, E.A. Allam, R. Elsaman, A. El-Taher, Fabrication and characterization of phosphotungstic acid-copper oxide nanoparticles-plastic waste nanocomposites for enhanced radiation-shielding, J. Alloys Compd. 803 (2019) 768–777.

[25] A.M. El-Khatib, M.I. Abbas, M.A. Elzaher, M.S. Badawi, M.T. Alabsy, G.A. Alharshan, D.A. Aloraini, Gamma attenuation coefficients of nano cadmium oxide/high density polyethylene composites, Sci. Rep. 9 (1) (2019) 16012.

[26] B.M. Abunahel, R.M. Ramli, K.M. Quffa, N.Z.N Azman, Effect of nanofibrous porosity on the X-ray attenuation properties of electrospun n-Bi2O3/epoxy–polyvinyl alcohol (PVA) nanofiber mats, Appl. Phys. A 124 (8) (2018) 540.

[27] A.H. Abdalsalam, E. Şakar, K.M. Kaky, M.H.A. Mhareb, B.C. Şakar, M.I. Sayyed, A. Gürol, Investigation of gamma ray attenuation features of bismuth oxide nano powder reinforced high-density polyethylene matrix composites, Radiat. Phys. Chem. 168 (2020) 108537.

[28] D.I. Tishkevich, T.I. Zubar, A.L. Zhaludkevich, I.U. Razanau, T.N. Vershinina, A.A. Bondaruk, … A.V. Trukhanov, Isostatic hot pressed W–Cu composites with nanosized grain boundaries: microstructure, structure and radiation shielding efficiency against gamma rays, Nanomaterials 12 (10) (2022) 1642.

[29] Y. Karabul, O. İçelli, The assessment of usage of epoxy based micro and nano-structured composites enriched with Bi2O3 and WO3 particles for radiation shielding, Results Phys. 26 (2021) 104423.

[30] A. Elaouni, M. El Ouardi, A. BaQais, M. Arab, M. Saadi, H. Ait Ahsaine, Bismuth tungstate Bi 2 WO 6: a review on structural, photophysical and photocatalytic properties, RSC Adv. 13 (26) (2023) 17476–17494.

[31] R.A. Surmenev, R.V. Chernozem, I.O. Pariy, M.A. Surmeneva, A review on piezo-and pyroelectric responses of flexible nano-and micropatterned polymer surfaces for biomedical sensing and energy harvesting applications, Nano Energy 79 (2021) 105442.

[32] B. Mutlu, F. Demirci, M. Erginer, Ş. Duman, In vitro behavior of boron-doped baghdadite/poly (vinylidene fluoride) membrane scaffolds produced via non-solvent induced phase separation, Macromol. Biosci. 25 (9) (2025) e00619.

[33] C. Mitharwal, S. Malhotra, A. Bagla, M.K. Srivastava, S.M. Gupta, C.M.S. Negi, … S. Mitra, Performance of dopamine modified 0.5 (Ba0. 7Ca0. 3) TiO3-0.5 Ba (Zr0. 2Ti0. 8) O3 filler in PVDF nanocomposite as flexible energy storage and harvester, J. Alloys Compd. 876 (2021) 160141.

[34] E. Şakar, Ö.F. Özpolat, B. Alım, M.I. Sayyed, M. Kurudirek, Phy-X/PSD: development of a user friendly online software for calculation of parameters relevant to radiation shielding and dosimetry, Radiat. Phys. Chem. 166 (2020) 108496.

[35] M.I. Sayyed, Investigating the influence of Bi2O3 on the radiation-shielding properties of TiO2-Bi2O3-B2O3-TeO2 glasses using the Phy-X software, Opt. Quantum Electron. 56 (2) (2024) 171.

[36] Y.S. Alajerami, M.H.A. Mhareb, M.I. Sayyed, M.K. Hamad, F. Kodeh, M. Rashad, M. Mitwalli, Comprehensive study for radiation shielding features for Bi2O3–B2O3–ZnO composite using computational radioanalytical Phy-X/PSD, MCNP5, and SRIM software, Sci. Rep. 14 (1) (2024) 17700.

[37] I.G. Geidam, K.A. Matori, M.K. Halimah, K.T. Chan, F.D. Muhammad, M. Ishak, S.A. Umar, Oxide ion polarizabilities and gamma radiation shielding features of TeO2–B2O3–SiO2 glasses containing Bi2O3 using Phy-X/PSD software, Mater. Today Commun. 31 (2022) 103472.

[38] J.F. Ziegler, Stopping of energetic light ions in elemental matter, J. Appl. Phys. 85 (3) (1999) 1249–1272.

[39] M.S. Kanca, Y. Taşgın, D. Yılmaz, A.F. Pathman, Ö. Güler, The effect of high entropy oxide on radiation shielding parameters of erbium oxide doped glasses, Ceram. Int. 50 (9) (2024) 15600–15612.

[40] H.D. Betz, Charge states and charge-changing cross sections of fast heavy ions penetrating through gaseous and solid media, Rev. Mod. Phys. 44 (3) (1972) 465–539.

[41] W. Brandt, M.J.P.R.B. Kitagawa, Effective stopping-power charges of swift ions in condensed matter, Phys. Rev. B 25 (9) (1982) 5631–5637.

[42] F. Hubert, R. Bimbot, H. Gauvin, Range and stopping-power tables for 2.5–500 MeV/nucleon heavy ions in solids, At. Data Nucl. Data Tables 46 (1) (1990) 1–213.

[43] R.I. Mahdi, A.A. Shakaty, J.K. Hmood, M.M. Najm, N.J. Al-Bahnam, S.W. Harun, Nanostructured LNTO saturable absorber for generating multi-wavelength laser in Q-switched EDFL, Opt. Mater. 157 (2024) 116122.

[44] M.M. Najm, R.I. Mahdi, J.K. Hmood, H.H. Abdullah, A.H. Abdulhadi, S.W. Harun, Performance investigation and optimization of EDFL based on lithium niobate–Titanium oxide nanomaterial saturable absorber, Opt. Mater. 165 (2025) 117118.

[45] R.I. Mahdi, W.C. Gan, W.H. Abd Majid, Hot plate annealing at a low temperature of a thin ferroelectric P (VDF-TrFE) film with an improved crystalline structure for sensors and actuators, Sensors 14 (10) (2014) 19115–19127.

[46] R.I. Mahdi, W.C. Gan, W.H. Abd Majid, N.I. Mukri, T. Furukawa, Ferroelectric polarization and pyroelectric activity of functionalized P (VDF-TrFE) thin film lead free nanocomposites, Polymer 141 (2018) 184–193.

[47] R.I. Mahdi, W.C. Gan, N.A. Halim, T.S. Velayutham, W.A. Majid, Ferroelectric and pyroelectric properties of novel lead-free polyvinylidenefluoride-trifluoroethylene–Bi0. 5Na0. 5TiO3 nanocomposite thin films for sensing applications, Ceram. Int. 41 (10) (2015) 13836–13843.

[48] R.I. Mahdi, W.A. Majid, Piezoelectric and pyroelectric properties of BNT-base ternary lead-free ceramic–polymer nanocomposites under different poling conditions, RSC Adv. 6 (84) (2016) 81296–81309.

[49] M. Karnan, K. Lolupiman, M. Okhawilai, P. Pattananuwat, M. Shetty, S. Venkateshalu, … J. Qin, Nanoarchitechtonic marvels: pioneering one-pot synthesis of Bi2WO6 nanostructures for breakthrough in symmetric supercapacitor innovation, ACS Appl. Energy Mater. 7 (13) (2024) 5490–5500.

[50] H. Li, N. Li, M. Wang, B. Zhao, F. Long, Synthesis of novel and stable g-C3N4-Bi2WO6 hybrid nanocomposites and their enhanced photocatalytic activity under visible light irradiation, R. Soc. Open Sci. 5 (3) (2018) 171419.

[51] X. Lian, W. Xue, S. Dong, E. Liu, H. Li, K. Xu, Construction of S-scheme Bi2WO6/g-C3N4 heterostructure nanosheets with enhanced visible-light photocatalytic degradation for ammonium dinitramide, J. Hazard. Mater. 412 (2021) 125217.

[52] E. Pastor, M. Sachs, S. Selim, J.R. Durrant, A.A. Bakulin, A. Walsh, Electronic defects in metal oxide photocatalysts, Nat. Rev. Mater. 7 (7) (2022) 503–521.

[53] S. Das, T. Ohkubo, S. Kasai, Y. Kozuka, Deterministic influence of substrate-induced oxygen vacancy diffusion on Bi2WO6 thin film growth, Cryst. Growth Des. 21 (1) (2021) 625–630.

[54] R.M. Sternheimer, M.J. Berger, S.M. Seltzer, Density effect for the ionization loss of charged particles in various substances, At. Data Nucl. Data Tables 30 (2) (1984) 261–271.

[55] G. Schiwietz, P.L. Grande, Stopping of protons–Improved accuracy of the UCA model, Nucl. Instrum. Methods Phys. Res. B: Beam Interact. Mater. At. 273 (2012) 1–5.

[56] J.C. Eckardt, Energy loss and straggling of protons and helium ions traversing some thin solid foils, Phys. Rev. A 18 (2) (1978) 426–433.

[57] J.E. Valdés, G. aMartínez Tamayo, G.H. Lantschner, J.C. Eckardt, N.R Arista, Electronic energy loss of low velocity H+ beams in Al, Ag, Sb, Au and Bi, Nucl. Instrum. Methods Phys. Res. B: Beam Interact. Mater. At. 73 (3) (1993) 313–318.

[58] J. Shams-Latifi, E. Pitthan, P.M. Wolf, D. Primetzhofer, Experimental electronic stopping cross-section of tungsten bulk and sputter-deposited thin films for slow protons, deuterons and helium ions, Nucl. Mater. Energy 36 (2023) 101491.

[59] E. Ponomareva, E. Pitthan, R. Holeňák, J. Shams-Latifi, G.P. Kiely, D. Primetzhofer, A.E. Sand, Local electronic excitations induced by low-velocity light ion stopping in tungsten, Phys. Rev. B 109 (16) (2024) 165123.

[60] V. Dose, G. Sele, Das elektronische Bremsvermögen von Stickstoff und Sauerstoff für niederenergetische protonen, Z. Phys. At. Nucl. 272 (3) (1975) 237–243.

[61] H. Baumgart, W. Arnold, H. Berg, E. Huttel, G. Clausnitzer, Proton stopping powers in various gases, Nucl. Instrum. Methods Phys. Res. 204 (2–3) (1983) 597–604.

[62] G. Konac, S. Kalbitzer, C. Klatt, D. Niemann, R. Stoll, Energy loss and straggling of H and He ions of keV energies in Si and C, Nucl. Instrum. Methods Phys. Res. B: Beam Interact. Mater. At. 136-138 (1998) 159–165.

[63] J.A. Phillips, The energy loss of low energy protons in some gases, Phys. Rev. 90 (4) (1953) 532.

[64] S.N. Chen, S. Atzeni, M. Gauthier, D.P. Higginson, F. Mangia, J.R. Marques, … J. Fuchs, Proton stopping power measurements using high intensity short pulse lasers produced proton beams, Nucl. Instrum. Methods Phys. Res. A: Accel. Spectrom. Detect. Assoc. Equip. 740 (2014) 105–106.

[65] N.J. Al-Bahnam, R.I. Mahdi, A.I.A. Al-Numan, W.A Majid, Describing the differential inelastic inverse mean free path of PMMA polymer with the Mermin–Belkacem-Sigmund model: NJ Al-Bahnam et al, Indian J. Phys. 97 (9) (2023) 2599–2610.

[66] J. Cazaux, D. Gramari, Dispersion des plasmons de surface dans les films de carbone amorphe, J. Phys. Lett. 38 (5) (1977) 133–136.

[67] R.C. Fadanelli, M. Behar, L.C. Nagamine, M. Vos, N.R. Arista, C.D. Nascimento, … I. Abril, Energy loss function of solids assessed by Ion beam energy-loss measurements: practical application to Ta2O5, J. Phys. Chem. C 119 (35) (2015) 20561–20570.

[68] J. Mbagwu, Theoretical investigation of dosimeter accuracy for linear energy transfer measurements in proton therapy: a comparative study of stopping power ratios, Radiat. Phys. Chem. 227 (2025) 112354.

[69] T. Krist, P. Mertens, Stopping ratios for 30–330 keV light ions in materials with 57⩽ Z2⩽ 83, Nucl. Instrum. Methods Phys. Res. 218 (1–3) (1983) 821–826.

[70] A.J. Antolak, B.N. Handy, D.H. Morse, A.E. Pontau, Energy loss and straggling measurements of ions in solid absorbers, Nucl. Instrum. Methods Phys. Res. B: Beam Interact. Mater. At. 59-60 (1991) 13–17.

[71] H.H. Andersen, F. Besenbacher, H. Knudsen, Stopping power and straggling of 65–500 keV lithium ions in H2, He, CO2, N2, O2, Ne, Ar, Kr and Xe, Nucl. Instrum. Methods 149 (1–3) (1978) 121–127.

[72] D.C. Santry, R.D Werner, Stopping powers of C, Al, Si, Ni, Ag and Au for 7Li ions, Nucl. Instrum. Methods Phys. Res. B: Beam Interact. Mater. At. 5 (3) (1984) 449–454.

[73] S.K. Allison, C.S. Littlejohn, Stopping power of various gases for lithium ions of 100-450-kev kinetic energy, Phys. Rev. 104 (4) (1956) 959–961.

[74] M.A. Hamada, O.M. Sadek, W.K. Mekhamer, I.H. Saleh, M. Elsafi, Green synthesis and characterization of Bi2O3 nanoparticles as outstanding filler in polyester for radiation shielding performance, Sci. Rep. 15 (1) (2025) 40352, doi:10.1038/s41598-025-26415-0.

[75] M. Yılmaz, F. Akman, Gamma radiation shielding properties for polymer composites reinforced with bismuth tungstate in different proportions, Appl. Radiat. Isot. 200 (2023) 110994, doi:10.1016/j.apradiso.2023.110994.